Three-dimensional fault geometries and interactions within experimental models of multiphase extension

Martha Oliver Withjack, Alissa A. Henza, and Roy W. Schlische

ABSTRACT

We use experimental (analog) models to examine the three-dimensional (3-D) fault geometries and interactions that develop during two phases of noncoaxial extension. In the models, a homogeneous layer of wet clay undergoes two phases of extension whose directions differ by 45°. The resulting fault pattern varies significantly with depth. At shallow levels, second-phase normal faults accommodate most second-phase extension. At depth, both second-phase normal faults and reactivated, first-phase faults with oblique slip accommodate most second-phase extension. A variety of interactions occurs between first-phase and second-phase faults. One interaction involves the upward propagation of second-phase faults from tips of reactivated, blind, first-phase faults. These hybrid faults have deep segments that strike subperpendicular to the first-phase extension direction and shallow segments whose strike varies with depth, becoming increasingly subperpendicular to the second-phase extension direction at shallow levels. A second interaction involves the nucleation of second-phase normal faults on the surfaces of reactivated, first-phase faults. These splay faults propagate upward and laterally from their nucleation sites into the hanging walls of the first-phase faults. As they propagate, they commonly encounter and link with different first-phase faults. The resulting composite faults have zigzag geometries in both map and cross-sectional views. A third interaction involves either the termination of second-phase antithetic normal faults against or near first-phase faults or the offset of first-phase faults by second-phase antithetic normal faults. The 3-D fault patterns and interactions within our models closely resemble those within the Taranaki basin of offshore New Zealand and Milne Point on Alaska's North Slope.

Manuscript received May 19, 2016; provisional acceptance September 8, 2016; revised manuscript received November 30, 2016; final acceptance February 7, 2017.
DOI:10.1306/02071716090

AUTHORS

MARTHA OLIVER WITHJACK ~ *Department of Earth and Planetary Sciences, Rutgers, The State University of New Jersey, 610 Taylor Road, Piscataway, New Jersey 08854; drmeow3@yahoo.com*

Martha Oliver Withjack received her B.S. degree from Rutgers, The State University of New Jersey, and her Ph.D. from Brown University. She worked in the petroleum industry as a research scientist and technical specialist for 22 years. In 2000, Dr. Withjack joined the faculty at Rutgers, as a professor in the Department of Earth and Planetary Sciences.

ALISSA A. HENZA ~ *Department of Earth and Planetary Sciences, Rutgers, The State University of New Jersey, 610 Taylor Road, Piscataway, New Jersey 08854; present address: Statoil Gulf Services LLC, 2107 City West Blvd, Houston, Texas, 77042; ahenza@gmail.com*

Alissa A. Henza received her B.S. degree from Cornell University in 2003 and her Ph.D. from Rutgers, The State University of New Jersey, in 2009. Since graduating, she has worked as both an exploration geologist and as a technical specialist in the oil and gas industry. Dr. Henza is currently a senior geologist at Statoil Gulf Services, L.L.C.

ROY W. SCHLISCHE ~ *Department of Earth and Planetary Sciences, Rutgers, The State University of New Jersey, 610 Taylor Road, Piscataway, New Jersey 08854; schlisch@eps.rutgers.edu*

Roy W. Schlische is a professor of structural geology at Rutgers, The State University of New Jersey. He received a B.A. degree from Rutgers, and a Ph.D. from Columbia University. His research interests include extensional tectonics, fault population studies, experimental modeling, and basin inversion. He has taught courses in structural geology, tectonics, field geology, introductory geology, economic geology, rift basins, and structural modeling.

ACKNOWLEDGMENTS

The authors thank Iain Sinclair for his insightful and thought-provoking conversations and for his inspiration to conduct this research. We also thank Mike Durcanin and Zul Zulfitriadi for their assistance with developing the serial section technique and Hemal Vora for preparing the serial sections. Finally, we thank Oliver Duffy and Peter Hennings for their careful and thoughtful reviews of the manuscript. This work was funded, in part, by the National Science Foundation (EAR-0838462) and generous support from Husky Energy. The authors also gratefully acknowledge Schlumberger for their donation of the Petrel 3D visualization software to Rutgers, The State University of New Jersey.

EDITOR'S NOTE

Color versions of Figures 1–18 can be seen in the online version of this paper.

INTRODUCTION

Many basins have undergone multiple phases of extension, commonly with differing extension directions. Examples include the petroliferous basins of the North Sea (e.g., Badley et al., 1988; Duffy et al., 2015), offshore Newfoundland (e.g., Sinclair, 1995), offshore New Zealand (e.g., Giba et al., 2012), onshore and offshore Thailand (e.g., Morley et al., 2004; Morley, 2016), the Northwest Shelf of Australia (e.g., Frankowicz and McClay, 2010), and the North Slope of Alaska (e.g., Nixon et al., 2014). Fault geometries and interactions are complex within these basins, varying laterally, with depth, and through time. Characterizing these complexities is essential to properly assess fluid flow properties and, thus, to identify pathways for hydrocarbon migration, define the geometry and integrity of hydrocarbon traps, and determine the likelihood of reservoir compartmentalization and directional variability of permeability.

Analog modeling studies, with their controlled boundary conditions and capability to observe deformation through time, provide a unique opportunity to systematically study fault development during multiphase extension. Thus far, modeling studies (Bonini et al., 1997; Keep and McClay, 1997; Dubois et al., 2002; Bellahsen and Daniel, 2005; Henza et al., 2010, 2011) have demonstrated that two factors strongly influence the map view fault patterns of basins with two phases of noncoaxial extension: (1) the angle between the two extension directions and (2) the degree of development of the first-phase fault population (i.e., the number, length, and displacement of the first-phase normal faults). These factors determine the likelihood of first-phase fault reactivation; the sense of slip on the reactivated faults; and the attitude, number, and length of new normal faults that form during the second phase of extension. The goal of this study is to supplement these prior modeling studies by focusing on the three-dimensional (3-D) variability of the fault patterns produced by two phases of noncoaxial extension. Specifically, we use analog models to investigate how the style and type of faulting (i.e., newly formed normal faults versus reactivated normal faults with oblique slip), the geometry and displacement of the faults, and the interactions between the first-phase and second-phase faults change with depth.

As discussed below, our modeling study shows that the fault networks, geometries, and interactions associated with two phases of noncoaxial extension vary temporally, laterally, and with depth. Many individual faults are complex structures, composed of linked fault segments with differing strikes, dips, and senses of slip. The displacement distribution on these faults is also complex, reflecting the fault interactions that occur during the second phase of extension. The 3-D fault patterns and interactions within our models closely resemble those within the Taranaki basin of offshore New

Zealand and at Milne Point on Alaska's North Slope, corroborating previous interpretations (Giba et al., 2012; Nixon et al., 2014) for multiple phases of noncoaxial extension.

EXPERIMENTAL APPROACH

Modeling Materials

Wet clay and dry sand are the most commonly used experimental modeling materials. Large-scale deformation patterns are similar in clay and sand models with similar boundary conditions, but small-scale deformation patterns differ (Withjack and Callaway, 2000; Eisenstadt and Sims, 2005; Withjack and Schlische, 2006). Fault zones are much narrower in clay models (<0.1 mm; see Table 1 for unit conversions) than in sand models (>1.0 mm) (Withjack et al., 2007). Deformation is more uniformly distributed within clay models (numerous minor to major faults and folds) than in sand models (mostly major faults). Additionally, fault propagation and linkage develop more gradually in clay models than in sand models, leading to the development of more fault-propagation folds, more relay ramps, and more sinuous fault traces in clay models than in sand models. In this study, we use wet clay as the modeling material to best capture the detailed 3-D fault geometries, interactions, and evolution during both phases of extension. The wet clay, composed mainly of kaolinite particles (<0.005 mm in diameter) and water (~40% by weight), has a density of 1.55–1.60 g cm^{-3}. Its cohesion (~50 Pa) and coefficient of internal friction (~0.6) are appropriate to ensure dynamic similarity between the models and nature (e.g., Withjack and Callaway, 2000; Eisenstadt and Sims, 2005; Henza et al., 2010, 2011; Cooke and van der Elst, 2012).

Experimental Setup

The experimental setup is identical with that described in Henza et al. (2010, 2011). The base of the apparatus consists of an initially 8-cm-wide rubber sheet attached to two rigid plates (one fixed and one mobile) (Figure 1A). A 0.5-cm-thick layer of polydimethylsiloxane silicone polymer (with a viscosity of ~10^4 Pa s; Weijermars, 1986; ten Grotenhuis et al., 2002) covers the rubber sheet (Figure 1B). A layer of wet clay (68 cm wide and 60 cm long) covers the polymer layer, the fixed plate, and the mobile plate. The clay layer is initially 3.5 cm thick over the polymer layer and 4 cm thick over the rigid plates. The layer of silicone polymer decouples the clay layer from the rubber sheet, allowing the base of the clay layer to move vertically during deformation. During the experiment, the displacement of the mobile plate stretches the rubber sheet and the overlying silicone polymer. In response, the clay above the silicone polymer also stretches, producing a broad region of subsidence and normal faulting. The displacement rate is 4 cm hr^{-1}; the total displacement magnitude is 3.5 cm for each phase of deformation.

Following Withjack and Jamison (1986), we define α as the angle (measured clockwise) between the long axis of the rubber sheet and the displacement direction of the mobile plate (Figure 1A). The displacement direction during the first phase of deformation (α_1) is 45°, and the displacement direction during the second phase (α_2) is 135° (Figure 1A). As discussed in Withjack and Jamison (1986), this 90°-clockwise rotation of the displacement directions from the first phase to the second phase of deformation corresponds to a 45°-clockwise rotation of the initial extension directions (i.e., $E_1 = 67.5°$, $E_2 = 112.5°$) (Figure 1A).

The two models described in this study are identical, with three exceptions (Figure 1B). (1) Model A is composed of a single clay layer, whereas model B is composed of multiple colored (but mechanically identical) clay sublayers. (2) In model A, no deposition occurs during the experiment, whereas in model B, infill deposition occurs after the first phase of deformation and after the second phase of deformation. We simulate infill deposition by completely filling the

Table 1. Conversion Factors for Modeling Parameters

Parameter	Conversion Factor
Grain size and fault zone width; spacing of serial sections	1 mm = 0.039 in.
Dimensions of modeling apparatus	1 cm = 0.39 in.
Density of wet clay	1 g cm^{-3} = 0.036 lb $in.^{-3}$
Cohesion of wet clay	1 Pa = 0.000145 lb_f $in.^{-2}$ (psi)
Dynamic viscosity of silicone putty	1 Pa s = 0.000145 lb_f s $in.^{-2}$
Displacement rate	1 cm hr^{-1} = 0.394 in. hr^{-1}

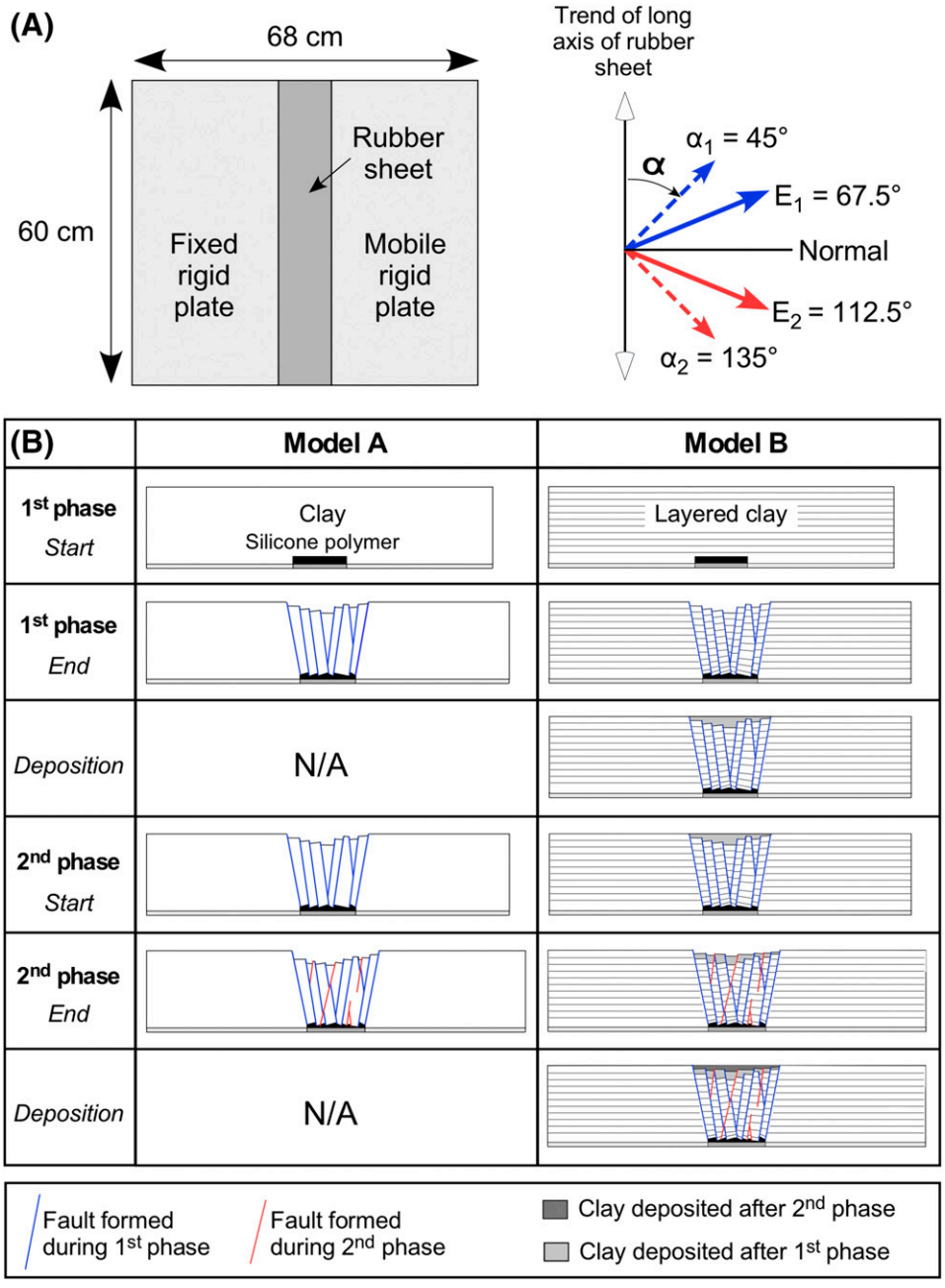

Figure 1. (A) Experimental setup in map where α is the angle measured clockwise from the long axis of the rubber sheet to the displacement direction (Withjack and Jamison, 1986). The first-phase displacement direction is α_1, and α_2 is the second-phase displacement direction. The initial maximum extension directions for phase 1 and phase 2 are E_1 and E_2, respectively. Note that the initial maximum extension direction is halfway between the displacement direction and the normal to the long axis of the rubber sheet. (B) Schematic cross-sectional views (orthogonal to the long axis of the rubber sheet) of models A and B. Vertical exaggeration is 3×. N/A = not applicable.

subsided regions with wet clay. (3) Model B is dried and preserved after the second phase of deformation and infill deposition. As discussed below, the preservation of model B allows us to closely examine the deformation both within and at the base of model B.

Analyses

We examine and photograph the top surfaces of model A (Figure 2) and model B (Figure 3) during both phases of extension, allowing us to track fault nucleation, propagation, and interaction. We also examine and photograph the bottom surface of model B (Figure 3C) after drying. Using this information, we determine the sense of slip of faults based on offset passive markers (i.e., superficial grooves on the top and bottom of the models created during construction) and the attitudes of corrugations on exposed fault surfaces (Hancock and Barka, 1987; Maltman, 1987; Granger et al., 2008; Henza et al., 2010, 2011) on the top and bottom of the models (Figures 2D, 3D).

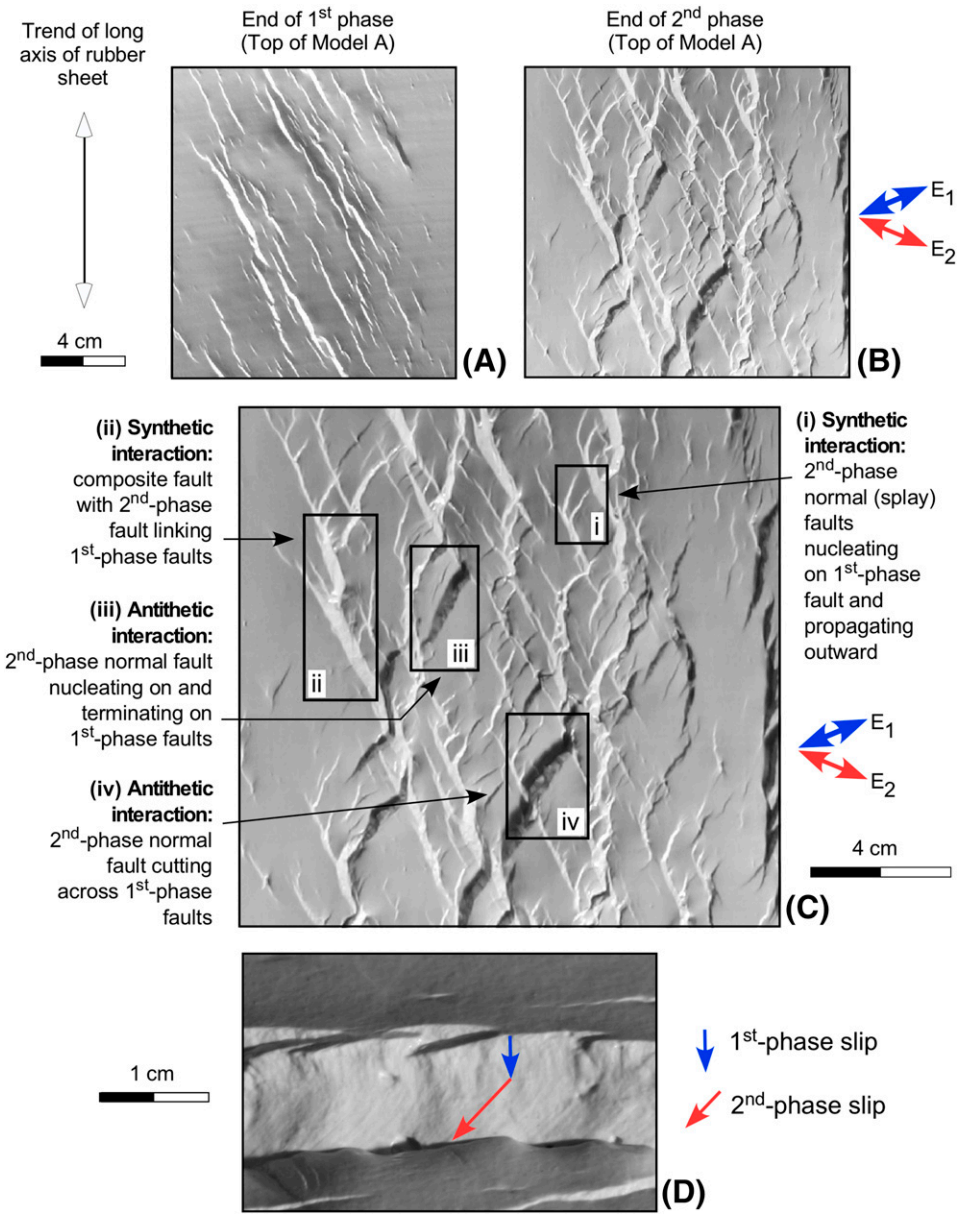

Figure 2. Photographs of the central part of the top surface of model A at (A) the end of the first phase and (B) the end of the second phase of extension. Faults dipping toward left appear dark; faults dipping toward right appear light. (C) Enlarged photograph of the central part of the top surface of model A at the end of the second phase of extension showing four common interactions (i–iv) between first-phase and second-phase faults. (D) Photograph of scarp of reactivated, first-phase fault from model A at the end of the second phase of extension. Corrugations on the fault surface indicate that fault had dip slip (normal) during the first phase and oblique slip (normal and right-lateral) during the second phase. E_1 = the initial maximum extension direction for phase 1; E_2 = the initial maximum extension direction for phase 2.

To define the deformation within model B, we use the serial section method described in Schlische et al. (2002) and Granger (2006). First, we prepare 21 serial sections (~1 mm apart), photograph the serial sections, and correct the photographic images for vertical and horizontal shrinkage of the clay during drying. We then import the corrected images into the Petrel software package, interpret several key horizons (along with those parts of faults offsetting the horizons) on each serial section (Figure 4A), and generate structure contour maps for each interpreted horizon (Figure 4B). These contour maps allow us to (1) map faults within the body of the analyzed model and use their strike to infer whether the faults likely developed during the first phase and/or second phase of deformation (Figure 5B), (2) correlate the first-phase and second-phase faults identified on the horizons with those in the serial sections (Figure 5A), and (3) define the interactions between the first-phase and second-phase faults in both map and cross-sectional views.

To supplement the serial section method, we make several vertical petrographic thin sections through model B. Because of the optical properties of the fault zones, examination of the thin sections allows us to detect small-scale deformation and

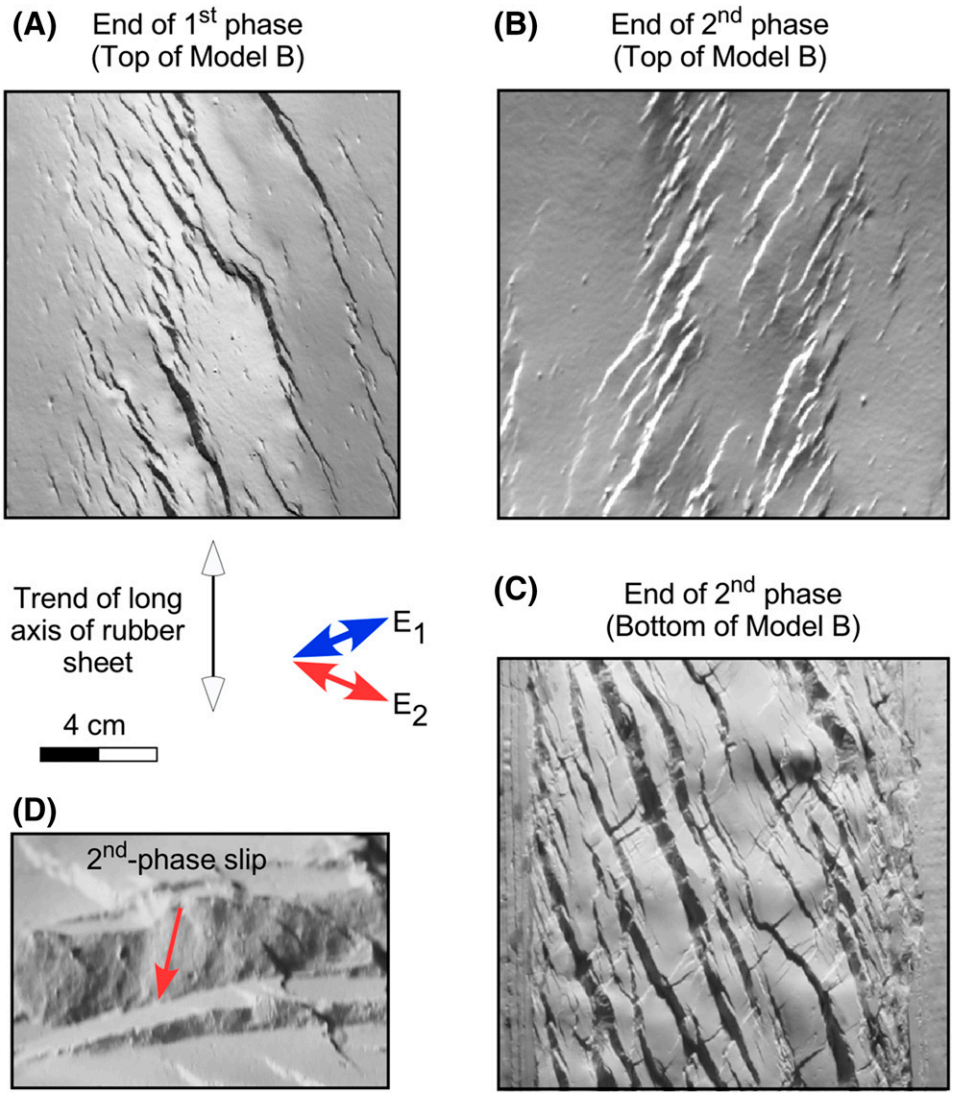

Figure 3. Photographs of part of the top of model B at (A) the end of first phase and (B) the end of second phase of extension. The top surface of model B after the second phase of extension is the top of the infill layer deposited after the first phase of extension. Faults dipping toward left appear dark; faults dipping toward right appear bright. (C) Photograph of part of the bottom surface of model B at the end of the second phase of extension. Faults dipping toward left appear dark; faults dipping toward right appear bright. (D) Close-up photograph of the bottom surface of model B (flipped vertically) showing corrugations on fault surfaces. Corrugations indicate that faults had oblique slip (normal and right-lateral) during the second phase of extension. E_1 = the initial maximum extension direction for phase 1; E_2 = the initial maximum extension direction for phase 2.

more precisely trace fault surfaces and define fault interactions within model B. Before deformation, most kaolinite grains within the model are subhorizontal, reflecting the construction of the clay model (e.g., Maltman, 1987). During deformation, kaolinite grains within the fault zones rotate and become subparallel to the fault zones, whereas kaolinite grains outside of the fault zones maintain their original horizontal orientation. Thus, under cross-polarized light, the fault zones in the thin sections appear bright relative to the unfaulted clay as the stage rotates (e.g., Maltman, 1987; Henza et al., 2011).

Constructing slip contour diagrams for faults within model B is difficult because the strike of the faults and the trend of their slip vectors are variable and generally oblique to the strike of the serial sections. Instead, we construct separation contour diagrams for several key faults by measuring the magnitude of fault separation for multiple horizons on the serial sections. Based on the strike of the faults and the trend of slip vectors observed on fault surfaces, we estimate that the magnitude of fault slip differs from that of the fault separation by less than 10%. These separation contour diagrams provide useful information about potential sites of fault nucleation (i.e., the sites of maximum fault slip), potential propagation directions (i.e., away from the sites of maximum fault slip), and fault interactions during the second phase of deformation (e.g., Rippon, 1985; Barnett et al., 1987; Nicol et al., 1996; Childs et al., 2003).

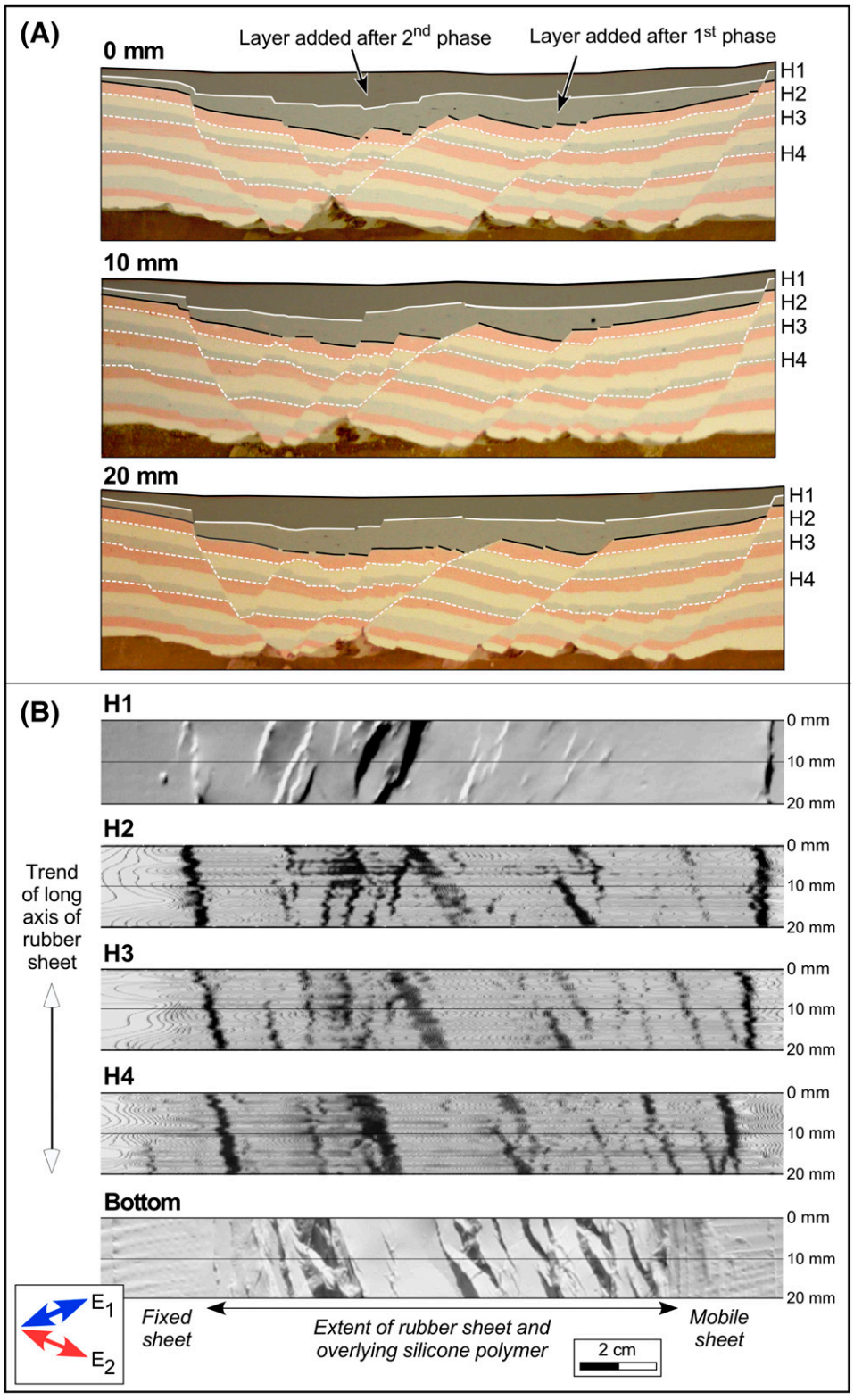

Figure 4. Serial section method used to construct three-dimensional geometry of faults. (A) Representative serial sections from model B after the second phase of extension. Cross sections are 3 of 21 serial sections from 2-cm-wide transect oriented orthogonally to long axis of rubber sheet. The numbers (top left) give the distance of the serial section from transect edge. The dashed white lines show digitized horizons H2–H4. The black line is the bottom of the first infill layer, and the solid white line is the top of the first infill layer (horizon H1). (B) Map views of horizons within transect. The top image is a photograph of H1. The bottom image is a photograph of the bottom surface of model B. Faults dipping toward left appear dark; faults dipping toward right appear bright. The three middle views show structure contour maps for H2–H4 created using the Petrel software package. Dipping fault surfaces, characterized by closely spaced contours, appear dark. E_1 = the initial maximum extension direction for phase 1; E_2 = the initial maximum extension direction for phase 2.

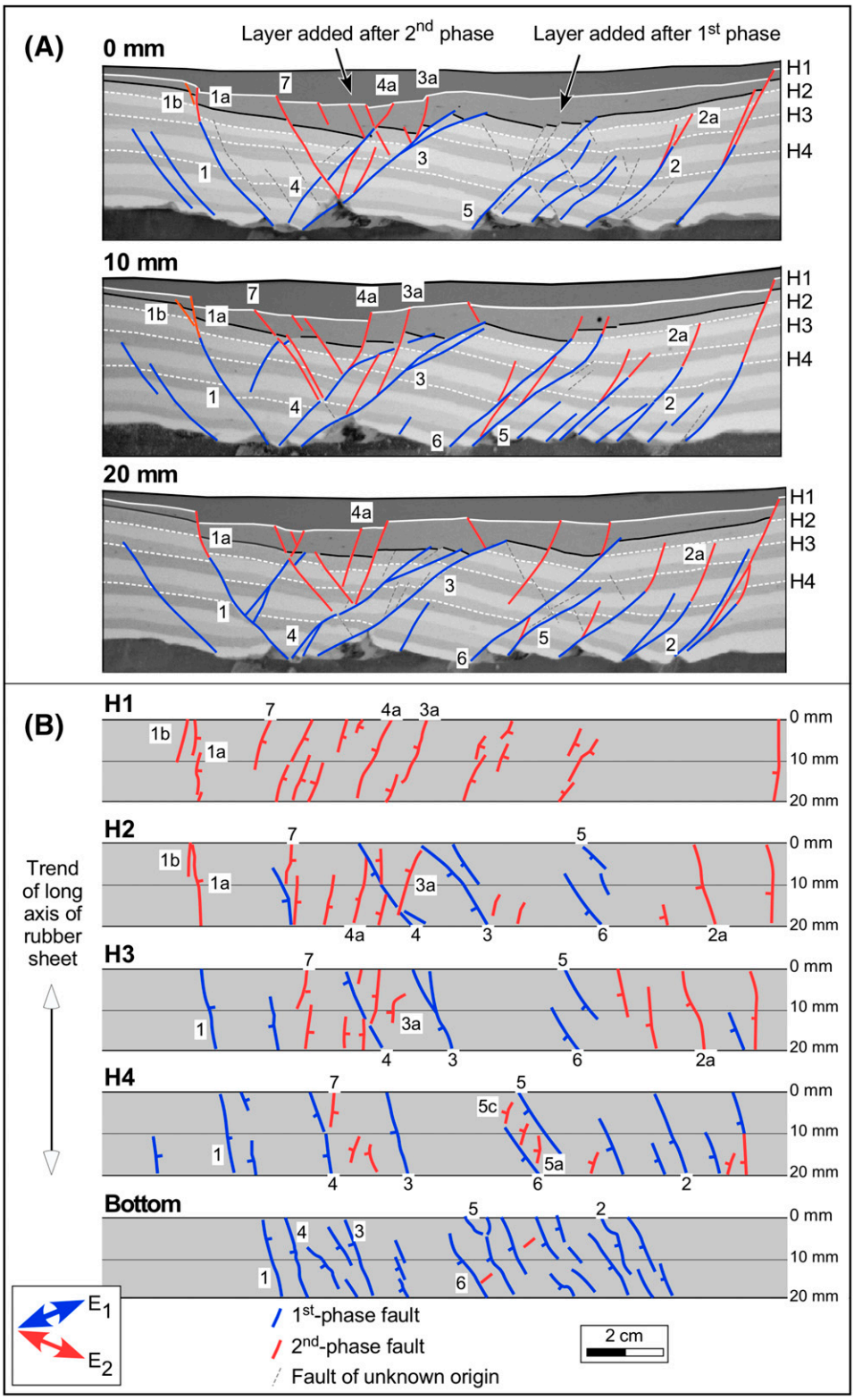

Figure 5. Interpreted faults using serial section method. (A) Serial sections for model B after the second phase of extension with fault interpretations. Cross sections are 3 of 21 serial sections from 2-cm–wide transect oriented orthogonally to long axis of a rubber sheet. The numbers (top left) give the distance of the serial section from the transect edge. The dashed white lines show digitized horizons H2–H4. The black line is the bottom of the first infill layer, and the solid white line is the top of the first infill layer (horizon H1). (B) Map view fault geometries for H1 to H4 and bottom surface of model B after the second phase of extension showing traces of footwall cutoffs of interpreted faults (tick marks on downthrown side). Numbers 1–7 refer to faults F1–F7 shown in Figures 6–10 and 11–14, respectively. E_1 = the initial maximum extension direction for phase 1; E_2 = the initial maximum extension direction for phase 2.

EXPERIMENTAL OBSERVATIONS

Fault Patterns on the Top Surface of Models A and B Resulting from First Phase of Extension

Normal faults form on the top surface of models A and B during the first phase of extension. Their strike is subperpendicular (±10°) to the initial direction of maximum horizontal extension (E_1) (Figures 2A, 3A) and, therefore, oblique to the long axis of the rubber sheet. For each model, most first-phase normal faults dip in the same direction, although the dip direction differs for the two models: toward the right in model A (Figure 2A) and toward the left in model B (Figure 3A). The first-phase fault patterns are similar to those in other models of oblique extension with $\alpha = 45°$ (e.g., Withjack and Jamison, 1986; Tron and Brun, 1991; McClay and White, 1995; Clifton et al., 2000; Schlische and Withjack, 2009; Henza et al., 2010, 2011).

Fault Patterns on Top Surface of Model A Resulting from Second Phase of Extension

Additional faulting occurs on the top surface of model A during the second phase of extension (Figure 2B, C). This faulting includes the formation of new, second-phase normal faults (striking approximately perpendicular to the second-phase extension direction) and the reactivation of first-phase faults (striking approximately perpendicular to the first-phase extension direction) with normal and right-lateral strike-slip components of displacement (Figure 2D). Many different types of interactions occur between the first-phase and second-phase faults on the top surface of model A during the second phase of extension. We classify these interactions into two broad categories, synthetic and antithetic. With synthetic-type interactions, the dip directions of the second-phase and first-phase faults are generally the same. With antithetic-type interactions, the dip directions of second-phase and first-phase faults are in opposing directions (Figure 2C).

The most common synthetic-type interaction on the top surface of model A involves the nucleation of second-phase normal (splay) faults on reactivated first-phase faults (Figure 2C, interaction i). During the second phase of extension, these second-phase splay faults propagate outward into the hanging walls of the reactivated first-phase faults. Some of these splay faults propagate into and link with different reactivated first-phase faults, producing a composite fault with a second-phase splay fault linking two reactivated, first-phase faults (Figure 2C, interaction ii). These composite faults have distinctive zigzag geometries in map view and are similar to those discussed in Henza et al. (2011). Thus, on the top surface of model A, most synthetic-type interactions between the second-phase and first-phase faults involve nucleation and linkage.

Antithetic-type interactions are less common on the top surface of model A than synthetic-type interactions. A few second-phase normal faults, dipping in the opposite direction as the first-phase faults, nucleate on reactivated first-phase faults (Figure 2C, interaction iii). As these second-phase normal faults propagate outward, some terminate against different first-phase faults, whereas others cut across and offset first-phase faults (Figure 2C, interaction iv). Thus, on the top surface of model A, most antithetic-type interactions between the second-phase and first-phase faults involve nucleation, termination, and offset.

Fault Patterns within Model B

During the second phase of extension, new normal faults offset the top surface of model B (i.e., the top surface of the infill layer deposited after the first phase of extension; Figure 1B). The strike of these second-phase normal faults is subperpendicular to the second-phase extension direction (Figure 3B).

Fault patterns within model B (Figures 4, 5) are far more complex than the simple fault pattern exposed on its top surface (Figure 3B). Many faults within model B have strikes that are subperpendicular to the first-phase extension direction (Figures 4B, 5B). These faults are most abundant near the base of the model, and many offset the bottom surface of the clay (Figure 3C). Based on corrugations on the exposed fault surfaces (Figure 3D), these faults have oblique slip with normal and right-lateral strike-slip components. Thus, most faults within model B with strikes subperpendicular to the first-phase extension direction are likely first-phase normal faults reactivated with oblique slip during the second phase of

extension. Other faults within model B have strikes that are subperpendicular to the second-phase extension direction (Figures 4B, 5B). These faults are most abundant near the top of the model, and many offset the top surface of the model (prior to the addition of the second infill layer). Based on corrugations on the exposed fault surfaces, these faults have normal slip. Thus, most faults within model B with strikes subperpendicular to the second-phase extension direction are likely new, second-phase normal faults. Finally, the strike of many faults within model B is oblique to both the first-phase and second-phase extension directions (Figures 4B, 5B). As discussed below, many of these faults are likely second-phase faults that propagate upward from the tips of reactivated, blind, first-phase faults during the second phase of extension.

Fault Interactions within Model B during the Second Phase of Extension

A variety of interactions occurs between the first-phase and second-phase faults within model B during the second phase of extension. We use serial sections, petrographic thin sections, structure contour maps, and photographs of the top and bottom surfaces of model B to identify these interactions and to define their 3-D characteristics. To demonstrate these interactions, we describe the attributes of faults F1 to F7 (locations given in Figure 5B).

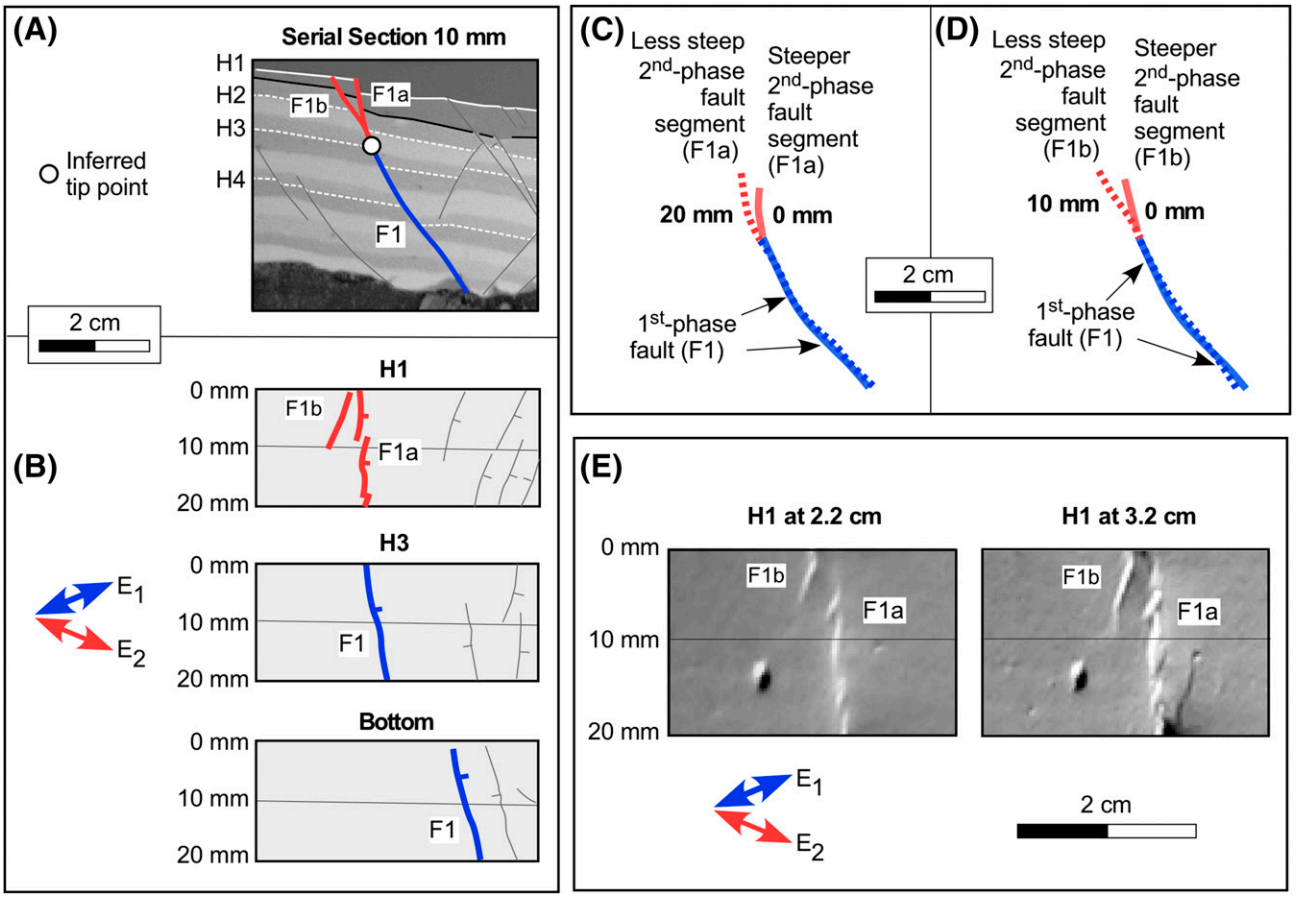

Figure 6. Geometry of hybrid fault with segments F1, F1a, and F1b. See Figure 5 for locations. (A) Part of serial section 10 mm. Second-phase fault segments (F1a and F1b) emanate from the inferred tip point of first-phase fault F1. All other faults are shown with thin gray lines. (B) Map views of H1, H3, and bottom of model B showing traces of footwall cutoffs of first-phase fault F1 and second-phase faults F1a and F1b (tick marks show downthrown side). All other faults are shown with thin gray lines. (C) Direct comparison of the surface of F1/F1a for serial sections 0 (solid line) and 20 mm (dashed line). (D) Direct comparison of the surface of F1/F1b for serial sections 0 (solid line) and 10 mm (dashed line). (E) Photographs of the surface of model B (i.e., H1) during the second phase of extension at 2.2 and 3.2 cm of displacement of the moving wall. E_1 = the initial maximum extension direction for phase 1; E_2 = the initial maximum extension direction for phase 2.

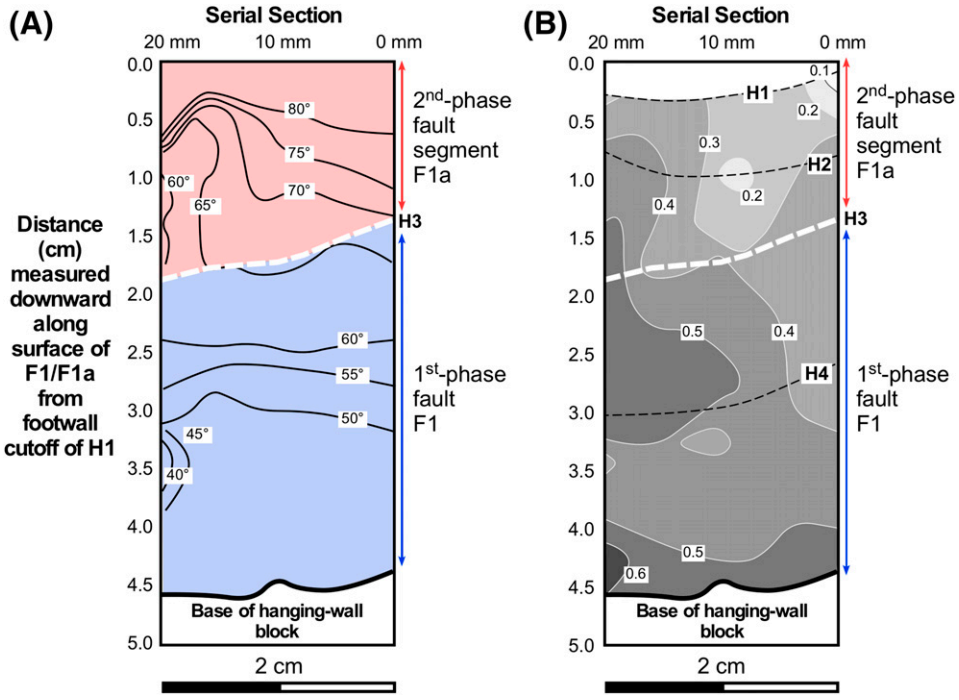

Figure 7. Characteristics of hybrid fault F1/F1a. (A) Apparent dip contour diagram for F1/F1a. True dip magnitudes differ by less than 1°. The white dashed line (near H3) is the inferred tip line for the first-phase fault F1. (B) Fault separation contour diagram for F1/F1a. Contours show the magnitude of separation (cm) at hanging wall locations projected onto vertical plane. The black dashed lines are hanging wall cutoffs for H1 through H4.

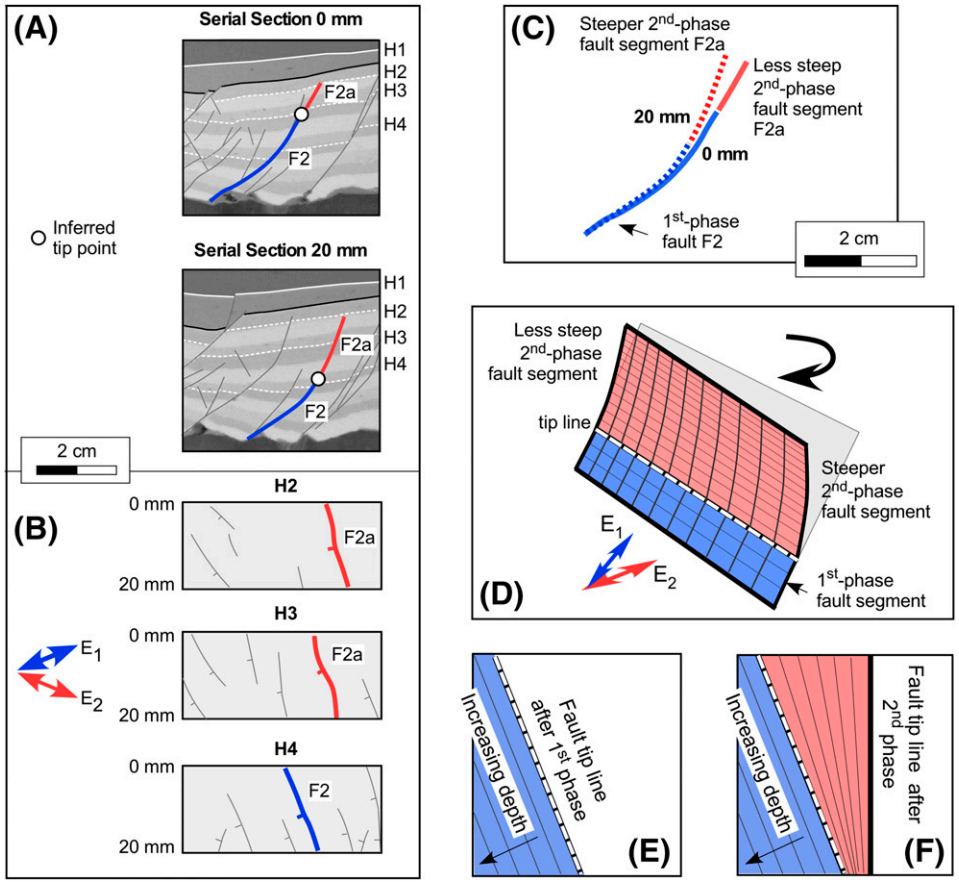

Figure 8. Geometry of hybrid fault with segments F2 and F2a. See Figure 5 for locations. (A) Parts of serial sections 0 and 20 mm. Second-phase fault segment F2a emanates from the inferred tip point of first-phase fault F2. All other faults are shown with thin gray lines. (B) Map views of H2, H3, and H4 showing traces of footwall cutoffs of first-phase fault F2 and second-phase fault F2a (tick marks show downthrown side). All other faults are shown with thin gray lines. (C) Direct comparison of the surface of F2 for serial sections 0 (solid line) and 20 mm (dashed line). (D) Schematic perspective diagram showing fault surface geometry of hybrid fault F2/F2a. Light gray plane above the tip line is the projected first-phase fault surface. Dip of shallow, second-phase segment changes along strike. (E) Schematic structure contour map on the surface of the hybrid fault after the first phase of extension. (F) Schematic structure contour map on the surface of the hybrid fault after the second phase of extension. E_1 = the initial maximum extension direction for phase 1; E_2 = the initial maximum extension direction for phase 2.

Emanation of Second-Phase Faults from Tips of Blind, First-Phase Faults

A common synthetic-type interaction within model B involves the emanation of new, second-phase faults from the upper tip lines of reactivated, blind, first-phase faults (i.e., faults that did not reach the model surface during the first phase of extension). Examples include first-phase fault F1 with its two emanating, second-phase fault segments F1a and F1b (Figures 6, 7) and first-phase fault F2 with its emanating, second-phase fault segment F2a (Figure 8). The hybrid faults resulting from this interaction have several distinctive characteristics.

The strike of their deep fault segments (i.e., F1 and F2) is subperpendicular to the first-phase extension direction, reflecting their formation during the first phase of extension (Figures 6B, 8B). The strike of their shallow fault segments (i.e., F1a, F1b, and F2a) changes with depth, ranging from oblique to both extension directions near the deep, first-phase fault segments to subperpendicular to the second-phase extension direction near the top surface of the model (Figures 6B, 8B). This upward clockwise rotation of strike reflects the upward propagation of the hybrid faults during the second phase of extension.

The dip of the deep segments of the hybrid faults is moderate and relatively uniform along strike (Figures 6C, D; 7A; 8C). The dip of their shallow fault segments ranges from moderate to subvertical and changes systematically along strike depending on the dip direction of the shallow segments. For example, the dip of right-dipping fault segments F1a and F1b increases toward serial section 0 mm (Figures 6C, D; 7A), whereas the dip of left-dipping fault segment F2a increases toward serial section 20 mm (Figure 8C). These changes in dip magnitude along strike accommodate the upward clockwise rotation of strike of the shallow segments of the hybrid faults during the second phase of extension (Figure 8D–F).

Separation varies significantly on the surfaces of the hybrid faults (e.g., F1/F1a; Figure 7B). Generally, separation is greatest at depth where fault

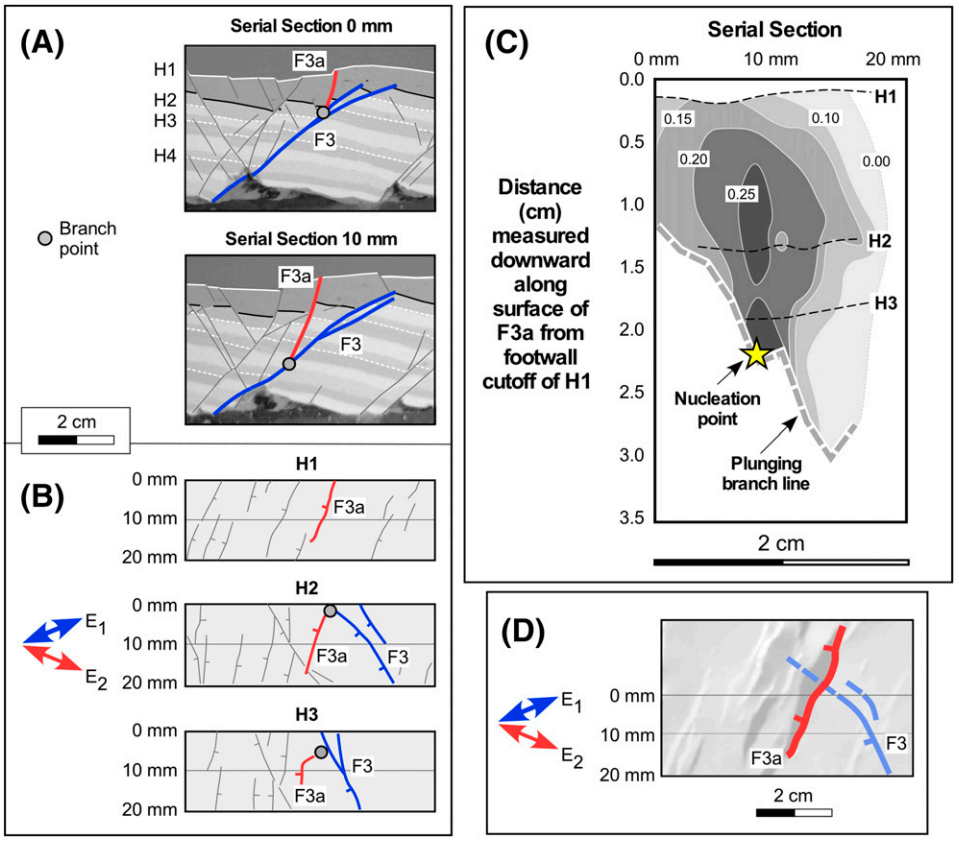

Figure 9. Characteristics of faults F3 and F3a. See Figure 5 for locations. (A) Parts of serial sections 0 and 10 mm. Second-phase splay fault F3a nucleates on reactivated first-phase fault F3 and propagates upward into its hanging wall. All other faults are shown with thin gray lines. (B) Map views of H1, H2, and H3 with traces of footwall cutoffs of first-phase fault F3 and second-phase splay fault F3a (tick marks show downthrown side). All other faults are shown with thin gray lines. (C) Fault separation diagram for F3a. Contours show magnitude of separation (cm) at hanging wall locations projected onto vertical plane. Black dashed lines are hanging wall cutoffs for H1 through H3. (D) Photograph of the part of top of model B after second phase of extension (i.e., top of first infill layer, H1) including the area of serial sections (0–20 mm) and the area beyond 0 mm. Lines show trace of footwall cutoff for the full length of F3a on H1 and the buried tip line of F3 (dashed where projected), which does not cut H1. E_1 = the initial maximum extension direction for phase 1; E_2 = the initial maximum extension direction for phase 2.

movement occurs during both phases of extension. Separation also varies along strike, especially on the shallow segments of the hybrid faults where fault propagation and interactions strongly influence fault development during the second phase of extension. For example, photographs of the top surface of model B (Figure 6E) show that the tips of second-phase faults segments F1a and F1b propagate laterally toward each other during the second phase of extension. Between serial section 10 mm and serial section 0 mm, the dip of F1a significantly increases (Figure 7A), the separation on F1a significantly drops (Figure 7B), and F1b becomes the dominant second-phase fault segment emanating from F1 (Figure 6E). These pronounced changes in fault separation and dip magnitude likely reflect an interaction between F1a and F1b (e.g., Nicol et al., 1996) during the second phase of extension.

Nucleation and Propagation of Second-Phase Splay Faults from First-Phase Faults

A second common synthetic-type interaction within model B involves the nucleation of new, second-phase normal faults on the surfaces of reactivated first-phase faults (Figures 9, 10). This interaction resembles the one observed on the top surface of model A where new, second-phase splay faults nucleate on reactivated first-phase faults and propagate outward (Figure 2C, interaction i). Within model B, second-phase splay faults propagate both laterally and upward from their nucleation sites into the hanging walls of the first-phase faults. For example, the fault separation diagram for second-phase splay fault F3a (Figure 9C) suggests that F3a nucleated on first-phase fault F3 near serial section 8 mm (i.e., the site of maximum separation) and then propagated upward and laterally toward serial section 0 mm and serial section 20 mm during the second phase of extension. As second-phase splay faults propagate upward into the first infill layer (i.e., the layer deposited after the first phase of extension), many lengthen substantially, unobstructed by the presence of first-phase faults. For example, after second-phase splay fault F3a propagated upward into the first infill layer, it propagated laterally across the buried tip line of first-phase fault F3 (Figure 9D).

Generally, the branch lines connecting second-phase splay faults with first-phase faults are moderately plunging. For example, the branch line connecting splay fault F3a with first-phase fault F3, although irregular, plunges approximately 50° to 60° (Figure 9C). For most reactivated first-phase faults, their separation changes across the branch lines with the second-phase splay faults. For example, the separation on first-phase fault F4 changes abruptly across its branch line with second-phase splay fault F4a (Figure 10). The transfer of displacement from reactivated first-phase fault (F4) to the overlying, second-phase splay fault (F4a) during the second phase of extension produces this abrupt reduction in separation.

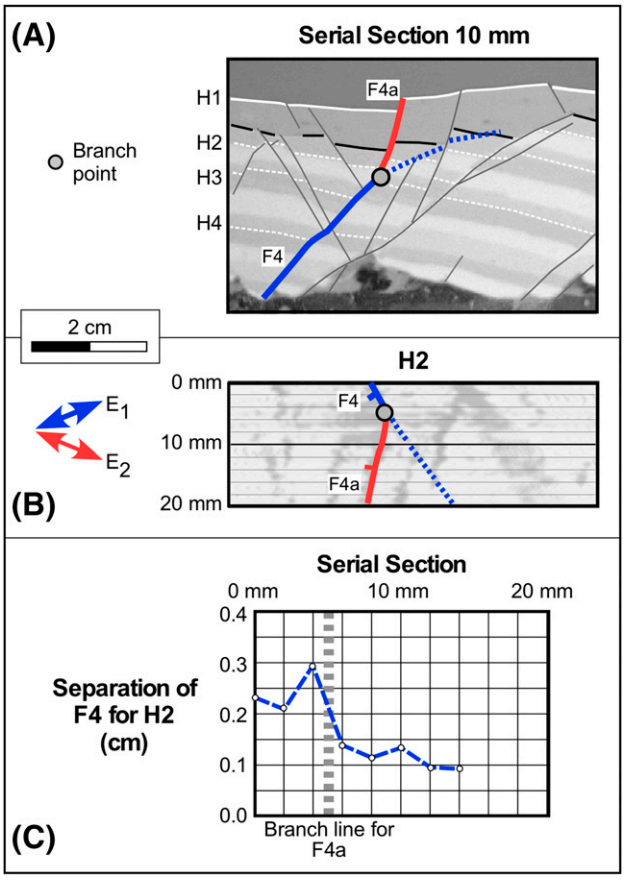

Figure 10. Interactions between first-phase fault F4 and second-phase splay fault F4a. See Figure 5 for locations. (A) Part of serial section 10 mm showing fault interpretations. Dashed line is a segment of F4 with limited reactivation during the second phase of extension. (B) Structure contour map on H2 showing fault interpretations (tick marks show downthrown side). (C) Graph of separation of fault F4 for horizon H2. Separation of F4 decreases abruptly across the branch line with F4a, reflecting transfer of displacement from F4 to F4a during the second phase of extension. E_1 = the initial maximum extension direction for phase 1; E_2 = the initial maximum extension direction for phase 2.

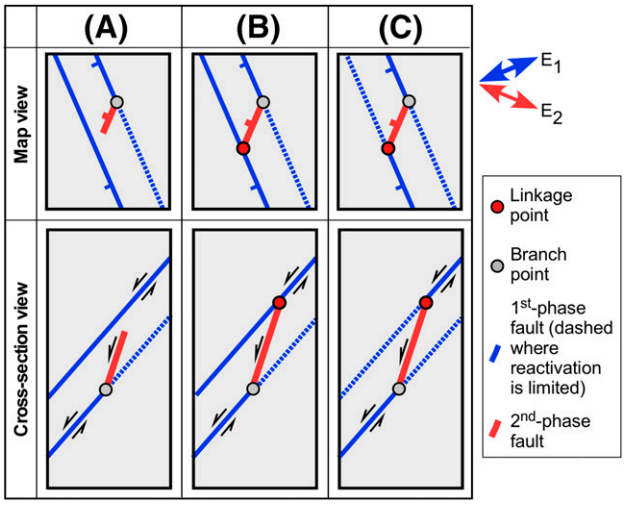

Figure 11. Schematic development of composite fault during the second phase of extension. In map views, tick marks show downthrown side. In cross-section views, arrows show dip-slip component. Reactivated first-phase faults also have right-lateral strike slip. (A) Second-phase splay fault nucleates on deep first-phase fault and propagates outward and upward into its hanging wall. First-phase fault segment above branch line (dashed line) has less slip than segment below branch line. (B) Second-phase splay fault propagates into and connects with shallow first-phase fault. (C) Second-phase splay fault links both first-phase faults. The first-phase segment below the linkage line (dashed line) has less slip than the segment above the branch line. E_1 = the initial maximum extension direction for phase 1; E_2 = the initial maximum extension direction for phase 2.

Linkage of Second-Phase and First-Phase Faults

As second-phase splay faults propagate upward and laterally from deep, reactivated first-phase faults during the second phase of extension, many encounter and link with overlying, shallow first-phase faults (Figure 11). The resulting composite faults, consisting of multiple hard-linked first-phase and second-phase fault segments, have zigzag geometries in both map and cross-sectional views (Figure 11). These faults closely resemble the composite faults present on the surface of model A (Figure 2B, interaction ii). Although many composite faults within model B consist of a single, second-phase splay fault linking two first-phase faults, others consist of multiple, second-phase splay faults that link two or more first-phase faults. For example, during the second phase of extension, second-phase splay faults F5a, F5b, and F5c branch from first-phase fault F5, propagate upward and outward, and link with first-phase fault F6 (Figure 12). Generally, the linkage lines between the splay faults and the overlying first-phase faults are moderately to steeply plunging, approximately 60° to 70° (Figure 13B).

Separation on the reactivated first-phase faults generally changes abruptly near the branch lines and linkage lines with the second-phase splay faults (Figures 12, 13). These changes in separation reflect the transfer of displacement, via the splay faults, from

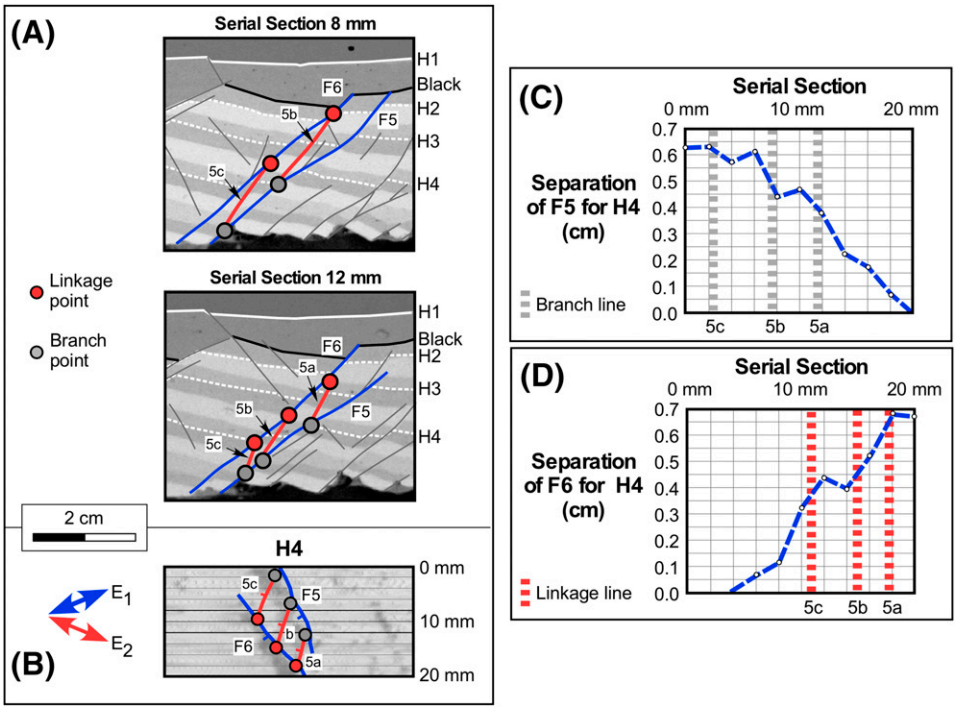

Figure 12. Characteristics of composite fault with first-phase faults F5 and F6 linked by second-phase faults F5a, F5b, and F5c. See Figure 5 for locations. (A) Parts of serial sections 8 and 12 mm with interpreted faults. (B) Interpreted structure contour map on horizon H4. The tick marks show the downthrown side of interpreted faults. (C) Graph showing separation of fault F5 for horizon H4. (D) Graph showing separation of fault F6 for horizon H4. E_1 = the initial maximum extension direction for phase 1; E_2 = the initial maximum extension direction for phase 2.

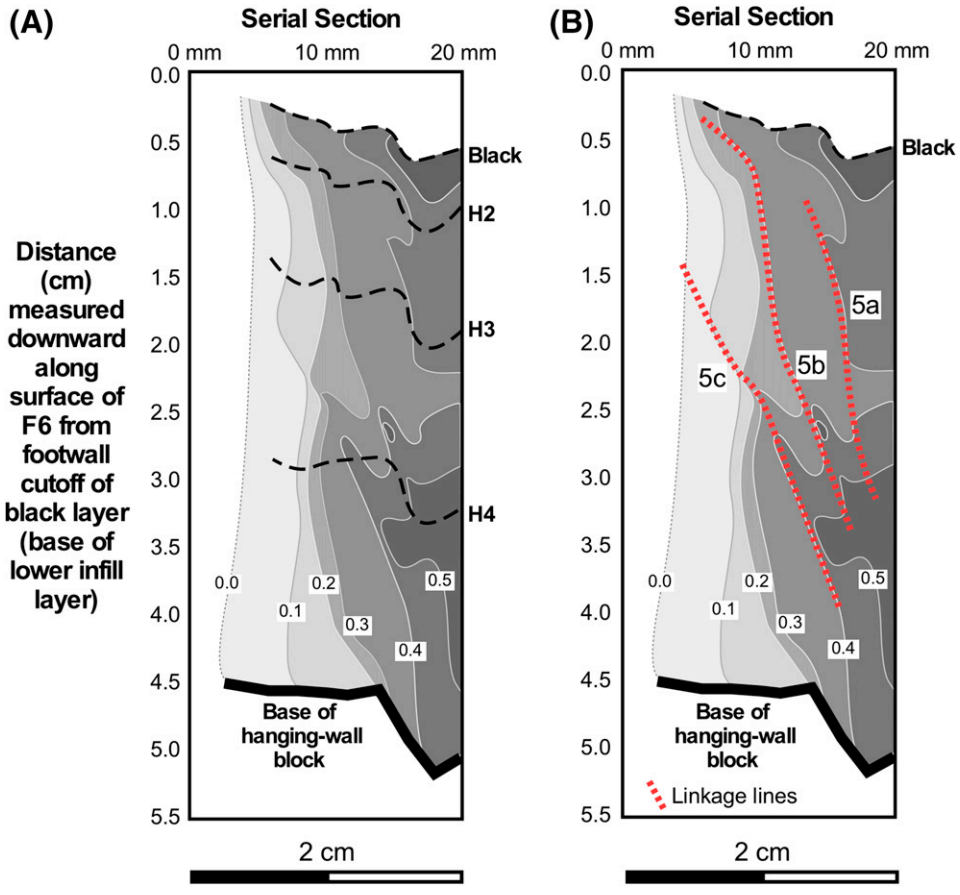

Figure 13. Fault separation diagrams for first-phase fault F6 (A) without and (B) with linkage lines for second-phase faults F5a, F5b, and F5c. Contours show magnitude of separation (cm) at hanging wall locations projected onto vertical plane. Thin, dashed black lines are hanging wall cutoffs for black horizon and horizons H2, H3, and H4. Separation increases (locally and generally) above linkage lines, reflecting transfer of displacement from F5 to F6 during second phase of extension.

the deeper first-phase fault to the shallower first-phase fault during the second phase of extension. For example, for horizon H4, separation on F5 decreases above the branch lines with F5a, F5b, and F5c (Figure 12C). Separation on F6, however, increases above the linkage lines with F5a, F5b, and F5c (Figure 12D), reflecting the transfer of displacement from F5 to F6. The separation diagram for F6 (Figure 13) shows that for all horizons, separation commonly increases above the linkage lines with F5a, F5b, and F5c.

Termination against and Offset of First-Phase Faults by Second-Phase Antithetic Faults

Antithetic-type interactions within model B involve both the termination of second-phase antithetic normal faults on or near first-phase faults and the offset of first-phase faults by second-phase antithetic normal faults (Figure 5A). Some second-phase antithetic normal faults exhibit both types of interaction with the same first-phase fault. For example, second-phase antithetic fault F7 terminates against or near first-phase fault F4 between serial sections 8 and 10 mm but cuts and offsets F4 between serial sections 8 and 0 mm (Figure 14).

The type of antithetic-type interaction depends, at least in part, on the separation of the second-phase antithetic fault relative to that of the reactivated first-phase fault. For example, the separation of second-phase antithetic fault F7 is least near serial section 10 mm and greatest near serial section 0 mm (Figure 14B). In contrast, the second-phase component of separation of reactivated first-phase fault F4 is greatest near serial section 10 mm and least near serial section 0 mm (assuming that the separation of second-phase splay fault F4a is a proxy for the separation of F4 during the second phase of extension) (Figure 14B). Fault F7 terminates against or near F4 between serial sections 8 and 10 mm where the separation of F7 is least and F4 is greatest but cuts and offsets F4 between serial sections 8 and 0 mm where the separation of F7 is greatest and F4 is least (Figure 14B). The amount of offset of F4 by F7 increases as the separation of F4a (and by proxy F4) decreases (Figure 14B). It is unclear whether the

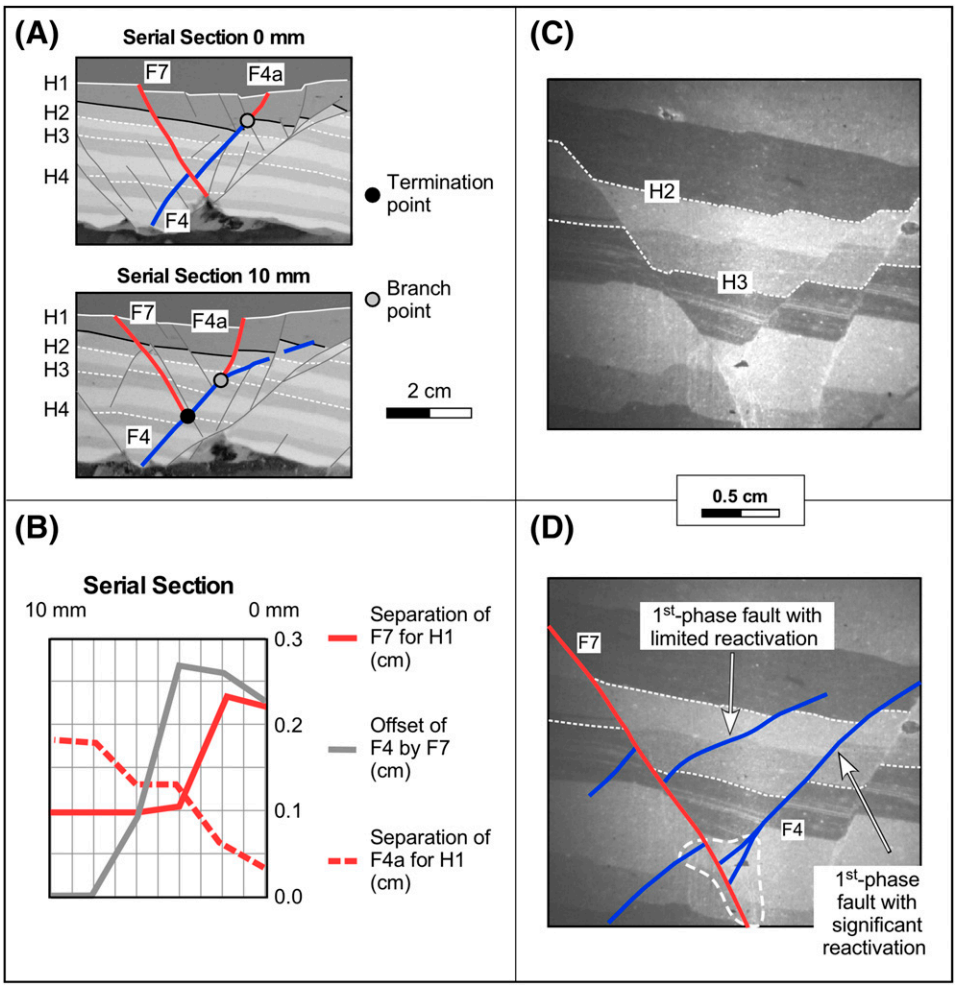

Figure 14. Relationship among second-phase antithetic fault F7, first-phase fault F4, and second-phase splay fault F4a. See Figure 5 for locations. (A) Serial sections 0 and 10 mm showing interactions among F7, F4, and F4a. (B) Plot showing separation of F7 for H1, offset of F4 by F7, and separation of F4a for H1 (a proxy for second-phase separation of F4). (C) Thin-section near serial section 0 mm without fault interpretation. (D) Same thin section with fault interpretation. Second-phase antithetic fault F7 cuts two first-phase faults, one with limited reactivation during second phase of extension and another (F4) with significant reactivation during the second phase of extension. A broad zone of deformation (white dashed outline) surrounds the intersection of F7 and F4.

increased slip on reactivated first-phase fault F4 inhibited the propagation and growth of second-phase antithetic fault F7 or whether the increased slip on F7 inhibited the reactivation of first-phase fault F4.

Thin sections from model B suggest that the size of the damage zone (i.e., the region with high fracture density) associated with an antithetic-type interaction depends on the amount of reactivation of the first-phase fault (Figure 14C, D). Damage zones are small where second-phase antithetic faults cut and offset first-phase faults with limited reactivation during the second phase of extension. Damage zones are large, however, where second-phase antithetic faults cut and offset first-phase faults with significant reactivation during the second phase of extension. For example, a broad region of deformation occurs near the intersection of second-phase antithetic normal fault F7 and reactivated first-phase faults F4 (Figure 14D), reflecting the activity of both faults during the second phase of extension.

Characteristics of Faults within Model B

A great variety of faults form within model B during the second phase of extension (Figure 15). Many are isolated, second-phase normal faults. Others, however, are complex structures, composed of linked first-phase and second-phase fault segments with differing strikes, dips, and senses of slip. At depth, hybrid faults have oblique slip and strike subperpendicular to the first-phase extension direction. At shallow levels, they have normal slip and strike subperpendicular to the second-phase extension direction. Composite faults have zigzag geometries in both map and cross-sectional views, reflecting abrupt changes in the strike and dip of their fault segments. Reactivated first-phase segments have oblique slip and strike subperpendicular to the first-phase extension direction, whereas second-phase segments have normal slip and strike subperpendicular to the second-phase extension direction.

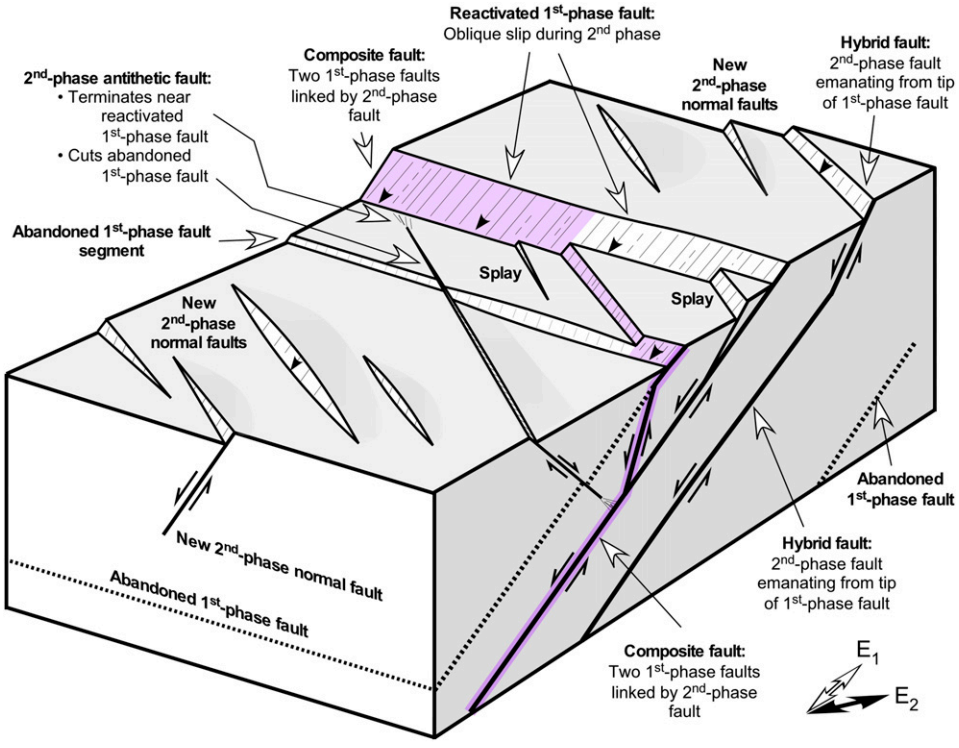

Figure 15. Summary diagram showing three-dimensional fault geometries and interactions associated with two phases of noncoaxial extension (initial maximum extension directions for phase 1 and phase 2 are E1 and E2, respectively). Arrows show separation on faults. New second-phase faults have predominantly normal displacement. Reactivated first-phase fault segments have normal and right-lateral strike-slip components of displacement.

For many faults within model B, the magnitude of separation changes substantially across branch lines and linkage lines, reflecting a transfer of displacement between first-phase and second-phase faults (Figures 10, 12). The separation contour diagrams for these faults (e.g., Figure 13) differ considerably from those associated with isolated normal faults with elliptical tip lines and contours surrounding central zones of maximum slip (e.g., Rippon, 1985; Barnett et al., 1987). Recent work by Duffy et al. (2015), using 3-D seismic data from the Norwegian North Sea, supports these modeling results. They have identified pronounced changes in separation across branch lines, reflecting the transfer of displacement between first-phase and second-phase faults during the second phase of extension.

APPLICATIONS

As described below, the fault geometries and interactions observed in 3-D seismic surveys from the Taranaki basin, offshore New Zealand, and from Milne Point, North Slope of Alaska, closely resemble those in our models.

Taranaki Basin, Offshore New Zealand

Using 3-D seismic data, Giba et al. (2012) defined the 3-D fault patterns within the Taranaki basin of offshore New Zealand. They concluded that two phases of noncoaxial extension affected the basin: an older east–west phase during the Late Cretaceous to early Eocene and a subsequent northwest–southeast phase during the early Pliocene (Figure 16A). The two extension directions differed by approximately 20°.

Numerous north-striking normal faults formed during the first phase of extension. During the second phase, new normal faults formed, many emanating from the upper tip lines of underlying first-phase faults. As these second-phase faults propagated upward, their strikes became increasingly subperpendicular to the second-phase extension direction. The resulting hybrid faults (e.g., the Parihaka fault; Figure 16A) have deep segments striking subperpendicular to the first-phase extension direction (i.e., north–south) and shallow segments striking subperpendicular to the second-phase extension direction (i.e., northeast–southwest). Furthermore, the dip of the shallow segments changes along strike. For example, the dip of the upper segments

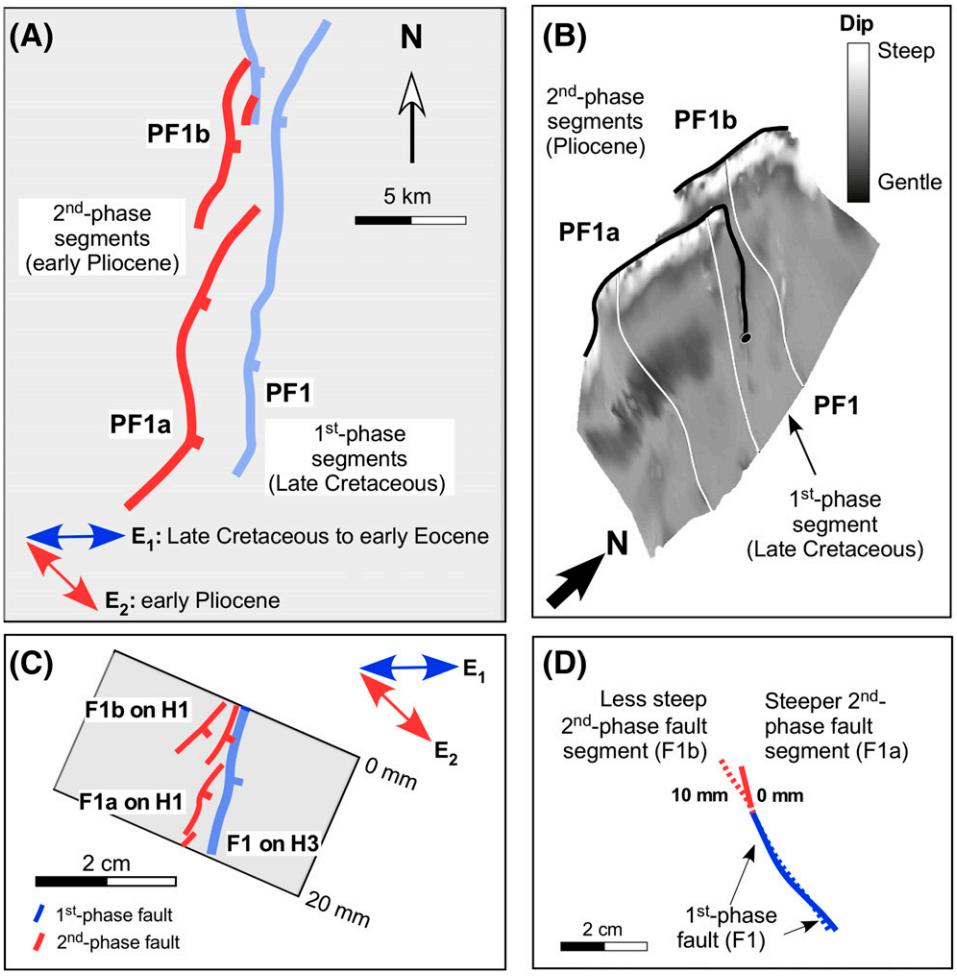

Figure 16. Comparison of fault patterns in Taranaki basin, offshore New Zealand (modified from Giba et al., 2012, and used with permission of Elsevier), with those from model B (reoriented). (A) Map of Parihaka fault showing traces of shallow, second-phase fault segments (PF1a and PF1b) formed during the early Pliocene and traces of deep, first-phase fault segment (PF1) active during the Late Cretaceous. (B) Perspective view of Parihaka fault (modified from Giba et al., 2012). Thin white lines highlight variations in fault shape, thick black lines are tip lines, and black dot is branch point. (C) Fault map of hybrid fault F1/F1a/F1b from model B showing footwall cutoff of first-phase fault F1 on deep horizon H3 and footwall cutoffs of second-phase faults F1a and F1b on shallow horizon H1. (D) Variation of shape of fault F1/F1b along strike and with depth. E_1 = the initial maximum extension direction for phase 1; E_2 = the initial maximum extension direction for phase 2.

of the Parihaka fault (i.e., segments PF1a and PF1b) (Figure 16B) systematically increases from the southwest to the northeast. The upward change of strike and the change in dip along strike of the shallow segments of the Parihaka fault closely resemble the upward change in strike (Figure 16C) and the change in dip along strike (Figure 16D) observed for the shallow segments of the hybrid faults in our models (e.g., second-phase segments F1a and F1b).

The results of our modeling study corroborate the conclusions of Giba et al. (2012) that, during the second-phase of extension, the deep segment of the Parihaka fault (i.e., PF1) was reactivated obliquely with normal and right-lateral components of slip. The shallow, second-phase fault segments (i.e., PF1a and PF1b) emanated from the buried, upper tip line of the deep segment of the Parihaka fault (Figure 16B). As they propagated upward, their strike changed, rotating approximately 15°–20° clockwise and becoming subperpendicular to the second-phase extension direction.

Milne Point, North Slope, Alaska

Using 3-D seismic data, Nixon et al. (2014) identified three distinct structural trends in the Milne Point region of the Alaskan North Slope. In the following discussion, we focus on two of those trends (Figures 17, 18). The younger (second-phase) trend developed during Jurassic to Early Cretaceous rifting and its associated north–northeast-south–southwest extension (E_2). It includes west–northwest-striking, moderately dipping normal faults (Figure 17A). The older (first-phase) trend is associated with deep, broad, northwest-trending horst and graben structures (Figure 17B). Individual northwest-striking

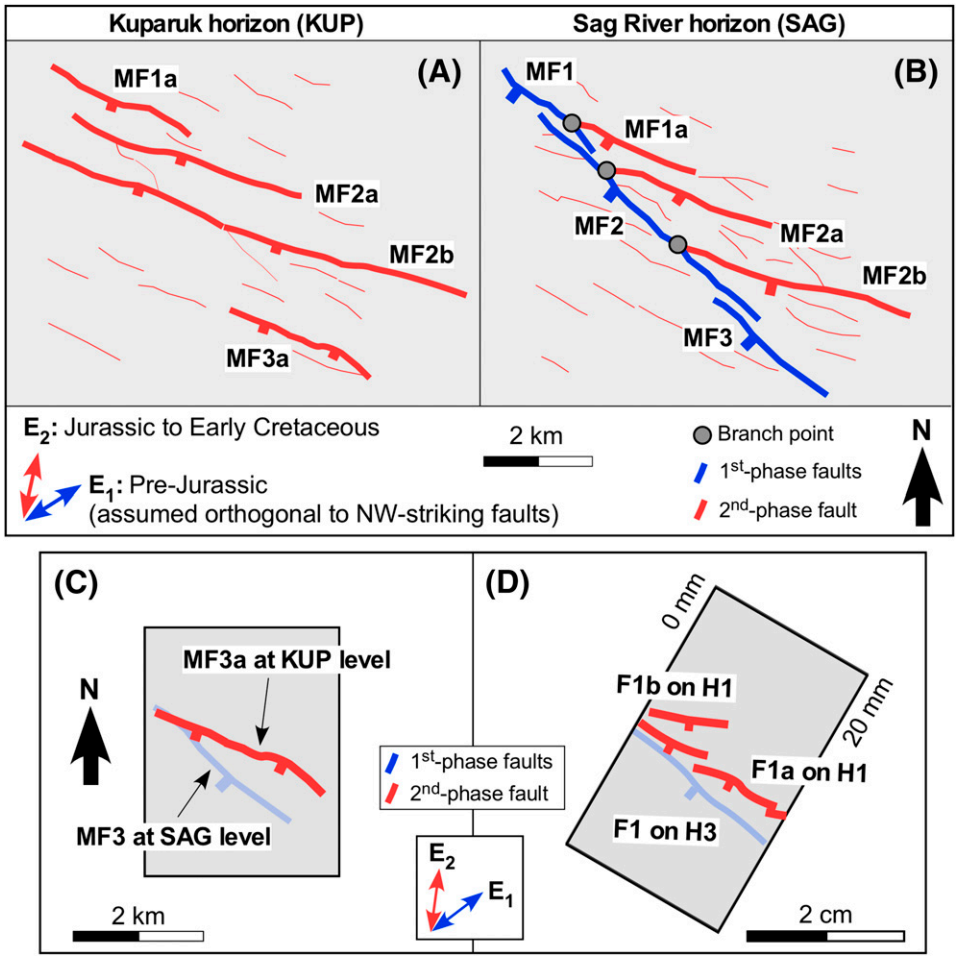

Figure 17. Maps comparing west–northwest- and northwest-striking faults from Milne Point, Alaska (modified from Nixon et al., 2014), with faults from model B (reoriented). (A) Younger, second-phase, west–northwest-striking normal faults cut Kuparuk Formation (KUP; Early Cretaceous). (B) Younger, second-phase, west–northwest-striking normal faults and older, first-phase, northwest-striking faults cut Sag River Formation (SAG; Late Triassic). Tick marks show downthrown side. (C) Example of hybrid fault from Milne Point showing footwall cutoffs of first-phase fault MF3 at SAG level and second-phase fault MF3a at KUP level. (D) Hybrid fault from model B showing footwall cutoffs of first-phase fault F1 on deep horizon H3 and second-phase faults F1a and F1b on shallow horizon H1. E_1 = the initial maximum extension direction for phase 1; E_2 = the initial maximum extension direction for phase 2.

faults have normal separation and steep dips (Figure 18D). Although the exact strain state associated with this phase of deformation is unclear, we assume that the extension direction (E_1) was approximately orthogonal to the northwest-striking faults (Figure 17B).

As observed by Nixon et al. (2014), faulting in the Milne Point region changes with depth. At shallow levels (i.e., the level of the Kuparuk Formation) (Figure 17A), west–northwest-striking faults are present, but northwest-striking faults are absent. At deeper levels (i.e., the level of the Sag River Formation) (Figure 17B), both west–northwest-striking and northwest-striking faults are present. This change in faulting with depth closely resembles that in our models where only second-phase faults are present at shallow levels (i.e., H1, the top of the first infill layer), but both first-phase and second-phase faults are present at deeper levels (i.e., H3) (Figures 5B, 17D). Our modeling results suggest that it is likely that the deep, northwest-striking structures at Milne Point were reactivated with oblique slip (normal and left-lateral strike-slip components) during the second phase of deformation, whereas the shallow, west–northwest-striking structures at Milne Point had predominantly normal slip during the second phase of deformation.

The interactions between the first-phase and second-phase faults in the Milne Point region also closely resemble those observed in our models. For example, fault MF3/MF3a (Figure 17C) appears to be a hybrid fault: its deep, northwest-striking segment (MF3) formed during the first phase of deformation, and its shallow, west–northwest-striking segment (MF3a) formed during the second phase of deformation. If MF3/MF3a is a hybrid fault similar to those in our models (e.g., Figure 17D), then its shallow segment (MF3a) emanated from the buried upper tip

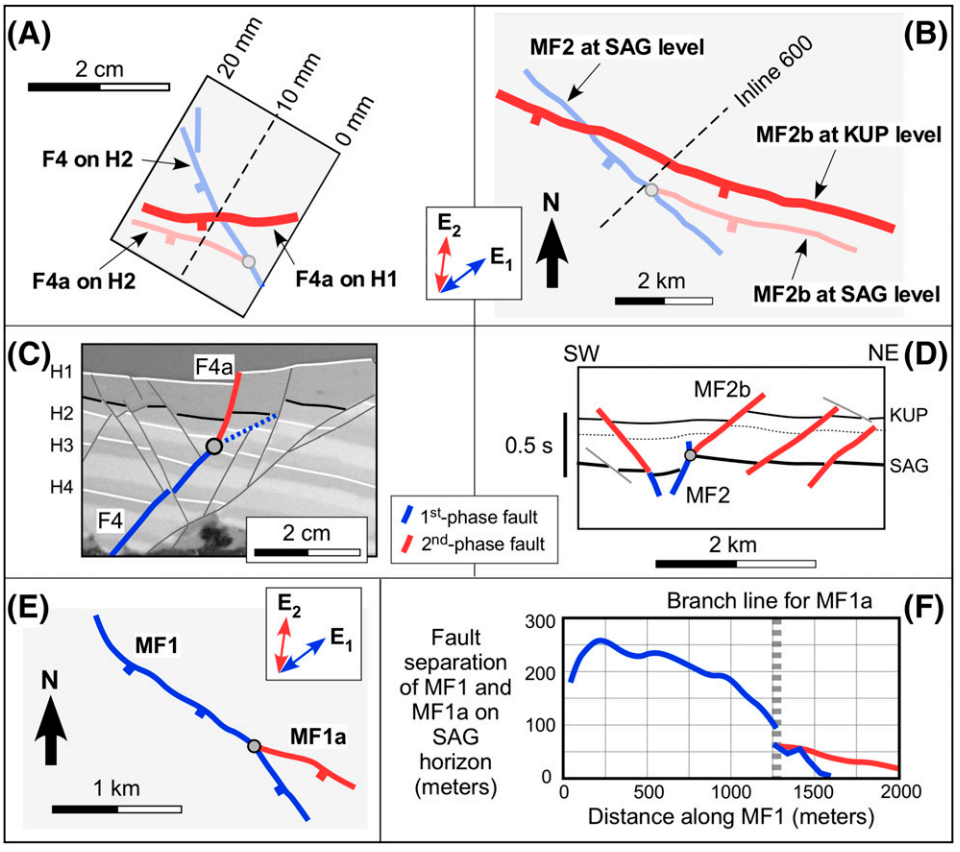

Figure 18. Comparison of splay fault interactions from model B (reoriented) with those from Milne Point, Alaska (modified from Nixon et al., 2014, and used with permission of AAPG). (A) Footwall cutoffs of first-phase fault F4 and second-phase splay fault F4a on deep horizon H2 (transparent) and footwall cutoff of F4a on shallow horizon H1 (bold). (B) Northwest-striking, first-phase fault MF2 and west–northwest-striking, second-phase splay fault MF2b at deep Sag River Formation (SAG) level (transparent) and MF2b at shallow Kuparuk Formation (KUP) level (bold). (C) Serial section 10 mm from model B showing first-phase fault F4 and second-phase splay fault F4a. (D) Interpreted line drawing of part of Inline 600 from Milne Point showing deep, northwest-striking, first-phase faults and west–northwest-striking, second-phase faults cutting KUP and SAG. Line displayed without vertical exaggeration assuming a velocity of 3500 m s^{-1} (11,480 ft s^{-1}). (E) Example of splay fault from Milne Point showing northwest-striking fault MF1 and west–northwest-striking splay fault MF1a at SAG level. (F) Plot showing separation of MF1 and MF1a on SAG horizon. Thick, dashed gray line is branch line for MF1a. E_1 = the initial maximum extension direction for phase 1; E_2 = the initial maximum extension direction for phase 2.

line of reactivated, northwest-striking, first-phase fault (MF3) during the second phase of deformation. As the shallow segment propagated upward, its strike rotated to become more orthogonal to the second-phase extension direction.

Nixon et al. (2014) observed that many of the west–northwest-striking normal faults at Milne Point splay from the older, northwest-striking structures (e.g., Figure 17B). These splay faults are similar to those observed in our models in several ways. The splay faults strike subperpendicular to the second-phase extension direction, they intersect the surfaces of first-phase faults (Figure 18A versus Figure 18B), and the displacement on the reactivated first-phase faults changes abruptly at the intersection/branch line (Figure 18E versus Figure 18F). Furthermore, the lengths of the splay faults increase significantly in the layers deposited after the first phase of deformation, propagating across the buried tip lines of the first-phase faults (Figure 18A versus Figure 18B). The splay faults at Milne Point differ from those observed in our models in that their dips are shallower than the dip of the reactivated first-phase faults, and they developed predominantly in the footwall, instead of hanging wall, of the reactivated first-phase faults (Figure 18C versus Figure 18D). We suggest that footwall splays, instead of hanging wall splays, developed at Milne Point because the reactivated, first-phase faults had steep dips compared with the gently dipping first-phase faults in model B.

DISCUSSION AND CONCLUSIONS

Our modeling results, together with observations from the Taranaki basin of offshore New Zealand and Milne Point on Alaska's North Slope, suggest the following.

1. The style and geometry of faulting can vary both laterally and with depth in basins affected by two phases of noncoaxial extension. At shallow levels, new normal faults (striking subperpendicular to the second-phase extension direction) are likely to accommodate most of the second-phase extension. At deep levels, both new normal faults and reactivated first-phase faults with oblique slip (striking subperpendicular to the first-phase extension direction) are likely to accommodate most of the second-phase extension.
2. Many types of fault interactions occur within basins with two phases of noncoaxial extension (Figure 15). (1) A common synthetic-type interaction involves the emanation and upward propagation of new, second-phase faults from the upper tip lines of reactivated, blind, first-phase faults during the second phase of extension. The resulting hybrid faults have distinctive characteristics. Their deep segments have oblique slip and strikes that are subperpendicular to the first-phase extension direction, whereas their shallow segments have normal slip and strikes that vary with depth, becoming increasingly subperpendicular to the second-phase extension direction at shallow levels. The dip of the shallow segments varies along strike to accommodate the upward rotation of strike. (2) Another common synthetic-type interaction involves the nucleation of new normal faults on the surfaces of reactivated first-phase faults. These splay faults propagate both upward and laterally from their nucleation sites into the hanging walls of the first-phase faults. The slip on the first-phase faults drops above the branch lines with the splay faults, reflecting the transfer of displacement from the first-phase fault to the splay fault during the second phase of extension. Footwall splays, instead of hanging wall splays, develop at Milne Point, Alaska, where the reactivated, first-phase faults are steeply dipping instead of gently dipping as are the reactivated, first-phase faults in our models. This suggests that the dip of the first-phase faults influences whether hanging wall or footwall splays develop during the second phase of extension. (3) As splay faults propagate upward and laterally from reactivated first-phase faults during the second phase of extension, they commonly encounter and link with overlying and/or outlying first-phase faults. The resulting composite faults, consisting of multiple hard-linked first-phase and second-phase fault segments, have zigzag geometries in both map and cross-sectional views. The slip magnitude on linked first-phase faults varies, changing abruptly near the branch lines and linkage lines with second-phase splay faults. These changes in slip magnitude reflect the transfer of displacement, via the splay faults, from the deeper first-phase faults to the shallower first-phase faults during the second phase of extension. (4) Common antithetic-type interactions involve either the termination of second-phase antithetic normal faults on or near first-phase faults or the offset of first-phase faults by second-phase antithetic normal faults. Antithetic-type interactions with termination are more likely to develop where slip on the second-phase antithetic fault is small relative to that on the reactivated, first-phase fault. In contrast, antithetic-type interactions with offset are more likely to occur where slip on the second-phase antithetic fault is large relative to that on the reactivated, first-phase fault. Broad regions of deformation (i.e., damage zones) can develop near the intersection of second-phase antithetic normal faults and reactivated, first-phase faults.
3. Individual faults within basins with two phases of noncoaxial extension are likely to be complex structures, composed of linked fault segments with strike, dip, and slip (magnitude and sense) that vary with depth and through time. Separation contour diagrams for these faults differ considerably from those associated with isolated normal faults, reflecting the fault interactions that occur during the second phase of extension.
4. Fault networks and, thus, the pathways for migrating hydrocarbons and the geometries of structural traps can vary significantly with depth in basins affected by two phases of noncoaxial extension. Additionally, fault interactions are likely to occur, affecting the integrity of hydrocarbon traps, the compartmentalization of reservoirs, and the directional variability of permeability. Fault damage zones can be especially large near the intersection of second-phase antithetic faults and reactivated first-phase faults.

REFERENCES CITED

Badley, M. E., J. D. Price, C. R. Dahl, and T. Agdestein, 1988, The structural evolution of the northern Viking Graben and its bearing upon extensional models of basin formation: Journal of the Geological Society, v. 145, p. 455–472, doi:10.1144/gsjgs.145.3.0455.

Barnett, J. A. M., J. Mortimer, J. H. Rippon, J. J. Walsh, and J. Watterson, 1987, Displacement geometry in the volume containing a single normal fault: AAPG Bulletin, v. 71, no. 8, p. 925–937.

Bellahsen, N., and J. M. Daniel, 2005, Fault reactivation control on normal fault growth: An experimental study: Journal of Structural Geology, v. 27, p. 769–780, doi:10.1016/j.jsg.2004.12.003.

Bonini, M., T. Souriot, M. Boccaletti, and J. P. Brun, 1997, Successive orthogonal and oblique extension episodes in a rift zone: Laboratory experiments with application to the Ethiopian Rift: Tectonics, v. 16, p. 347–362, doi:10.1029/96TC03935.

Childs, C., A. Nicol, J. J. Walsh, and J. Watterson, 2003, The growth and propagation of synsedimentary faults: Journal of Structural Geology, v. 25, p. 633–648, doi:10.1016/S0191-8141(02)00054-8.

Clifton, A. E., R. W. Schlische, M. O. Withjack, and R. V. Ackermann, 2000, Influence of rift obliquity on fault-population systematics: Results of clay modeling experiments: Journal of Structural Geology, v. 22, p. 1491–1509, doi:10.1016/S0191-8141(00)00043-2.

Cooke, M. L., and N. J. van der Elst, 2012, Rheologic testing of wet kaolin reveals frictional and bi-viscous behavior typical of crustal materials: Geophysical Research Letters, v. 39, L01308, doi:10.1029/2011GL050186.

Dubois, A., F. Odonne, G. Massonnat, T. Lebourg, and R. Fabre, 2002, Analogue modelling of fault reactivation: Tectonic inversion and oblique remobilization of grabens: Journal of Structural Geology, v. 24, p. 1741–1752, doi:10.1016/S0191-8141(01)00129-8.

Duffy, O. B., R. E. Bell, C. A.-L. Jackson, R. L. Gawthorpe, and P. S. Whipp, 2015, Fault growth and interactions in a multiphase rift fault network: Horda Platform, Norwegian North Sea: Journal of Structural Geology, v. 80, p. 99–119, doi:10.1016/j.jsg.2015.08.015.

Eisenstadt, G., and D. Sims, 2005, Evaluating sand and clay models: Do rheological differences matter?: Journal of Structural Geology, v. 27, p. 1399–1412, doi:10.1016/j.jsg.2005.04.010.

Frankowicz, E., and K. R. McClay, 2010, Extensional fault segmentation and linkages, Bonaparte Basin, outer North West Shelf, Australia: AAPG Bulletin, v. 94, no. 7, p. 977–1010, doi:10.1306/01051009120.

Giba, M., J. J. Walsh, and A. Nicol, 2012, Segmentation and growth of an obliquely reactivated normal fault: Journal of Structural Geology, v. 39, p. 253–267, doi:10.1016/j.jsg.2012.01.004.

Granger, A. B., 2006, Influence of basal boundary conditions on normal-fault systems in scaled physical models, master's thesis, Rutgers, the State University of New Jersey, New Brunswick, New Jersey, 121 p.

Granger, A. B., M. O. Withjack, and R. W. Schlische, 2008, Fault surface corrugations: Insights from scaled experimental models of extension (abs.), *in* Fault zones: Structure, geomechanics, and Fluid flow conference: London, Geological Society, London, September 16, 2008, p. 38.

Hancock, P. L., and A. A. Barka, 1987, Kinematic indicators on active normal faults in western Turkey: Journal of Structural Geology, v. 9, p. 573–584, doi:10.1016/0191-8141(87)90142-8.

Henza, A. A., M. O. Withjack, and R. W. Schlische, 2010, Normal-fault development during two phases of non-coaxial extension: An experimental study: Journal of Structural Geology, v. 32, p. 1656–1667, doi:10.1016/j.jsg.2009.07.007.

Henza, A. A., M. O. Withjack, and R. W. Schlische, 2011, How do the properties of a pre-existing normal-fault population develop during a subsequent phase of extension?: Journal of Structural Geology, v. 33, p. 1312–1324, doi:10.1016/j.jsg.2011.06.010.

Keep, M., and K. R. McClay, 1997, Analogue modeling of multiphase rift systems: Tectonophysics, v. 273, p. 239–270, doi:10.1016/S0040-1951(96)00272-7.

Maltman, A. J., 1987, Shear zones in argillaceous sediments—An experimental study, *in* M. E. Jones and R. M. F. Preston, eds., Deformation of sediments and sedimentary rocks: Geological Society, London, Special Publications 1987, v. 29, p. 77–87, doi:10.1144/GSL.SP.1987.029.01.08.

McClay, K. R., and M. J. White, 1995, Analogue modeling of orthogonal and oblique rifting: Marine and Petroleum Geology, v. 12, p. 137–151, doi:10.1016/0264-8172(95)92835-K.

Morley, C. K., 2016, The impact of multiple extension events, stress rotation, and inherited fabrics on normal fault geometries and evolution in the Cenozoic rift basins of Thailand, *in* C. Childs, R. E. Holdsworth, C. A.-L. Jackson, T. Manzocchi, J. J. Walsh, and G. Yielding, eds., The geometry and growth of normal faults: Geological Society, London, Special Publications 2016, v. 439, doi:10.1144/SP439.3.

Morley, C. K., C. Harayana, W. Phoosongsee, S. Pongwapee, A. Kornsawan, and N. Wonganan, 2004, Activation of rift oblique and rift parallel pre-existing populations during extension and their effect on deformation style: Examples from the rifts of Thailand: Journal of Structural Geology, v. 26, p. 1803–1829, doi:10.1016/j.jsg.2004.02.014.

Nicol, A., J. Watterson, J. J. Walsh, and C. Childs, 1996, The shapes, major axis orientations and displacement patterns of fault surfaces: Journal of Structural Geology, v. 18, p. 235–248, doi:10.1016/S0191-8141(96)80047-2.

Nixon, C. W., D. J. Sanderson, S. J. Dee, J. M. Bull, R. J. Humphreys, and M. H. Swanson, 2014, Fault interaction and reactivation within a normal-fault network at Milne Point, Alaska: AAPG Bulletin, v. 98, no. 10, p. 2081–2107, doi:10.1306/04301413177.

Rippon, J. H., 1985, Contoured patterns of the throw and hade of normal faults in the Coal Measures (Westphalian) north-east Derbyshire: Proceedings of the Yorkshire

Geological Society, v. 45, p. 147–161, doi:10.1144/pygs.45.3.147.

Schlische, R. W., and M. O. Withjack, 2009, Origin of fault domains and fault-domain boundaries (transfer zones and accommodation zones) in extensional provinces: Result of random nucleation and self-organized fault growth: Journal of Structural Geology, v. 31, p. 910–925, doi:10.1016/j.jsg.2008.09.005.

Schlische, R. W., M. O. Withjack, and G. Eisenstadt, 2002, An experimental study of the secondary deformation produced by oblique-slip normal faulting: AAPG Bulletin, v. 86, no. 5, p. 885–906.

Sinclair, I. K., 1995, Transpressional inversion due to episodic rotation of extensional stresses in Jeanne d'Arc Basin, offshore Newfoundland, *in* J. G. Buchanan and P. G. Buchanan, eds., Basin inversion: Geological Society, London, Special Publications 1995, v. 88, p. 249–271, doi:10.1144/GSL.SP.1995.088.01.15.

ten Grotenhuis, S. M., C. W. Passchier, and P. D. Bons, 2002, The influence of strain localization on the rotation behavior of rigid objects in experimental shear zones: Journal of Structural Geology, v. 24, p. 485–499, doi:10.1016/S0191-8141(01)00072-4.

Tron, V., and J.-P. Brun, 1991, Experiments on oblique rifting in brittle-ductile systems: Tectonophysics, v. 188, p. 71–84, doi:10.1016/0040-1951(91)90315-J.

Weijermars, R., 1986, Flow behaviour and physical chemistry of bouncing putties and related polymers in view of tectonic laboratory applications: Tectonophysics, v. 124, p. 325–358, doi:10.1016/0040-1951(86)90208-8.

Withjack, M. O., and S. Callaway, 2000, Active normal faulting beneath a salt layer: An experimental study of deformation patterns in the cover sequence: AAPG Bulletin, v. 84, no. 5, p. 627–651.

Withjack, M. O., and W. R. Jamison, 1986, Deformation produced by oblique rifting: Tectonophysics, v. 126, p. 99–124, doi:10.1016/0040-1951(86)90222-2.

Withjack, M. O., and R. W. Schlische, 2006, Geometric and experimental models of extensional fault-bend folds, *in* S. J. H. Buiter and G. Schreurs, eds., Analogue and numerical modelling of crustal-scale processes: Geological Society, London, Special Publications 2006, v. 253, p. 285–305, doi:10.1144/GSL.SP.2006.253.01.15.

Withjack, M. O., R. W. Schlische, and A. A. Henza, 2007, Scaled experimental models of extension: dry sand versus wet clay: Houston Geological Survey Bulletin, v. 49, no. 8, p. 31–49.